Direct observations of density-driven streamwise oriented vortices at a river confluence

Duguay Duguay[1,1], Pascale Biron[1,1], and Jay Lacey[2,2]

[1]Concordia University
[2]Université de Sherbrooke

November 30, 2022

Abstract

When rivers collide, complex three-dimensional large-scale coherent turbulent structures are generated along the confluence's mixing interface. These structures play important roles in mixing streamborne pollutants and suspended sediment, and have considerable bearing on the morphology and habitat quality of the postconfluent reach. A particular structure of great interest, streamwise orientated vortices (SOVs), were first detected in numerical simulations to form in pairs, one flanking each side of the mixing interface rotating in the opposite sense of the other. Since, it has proved difficult to detect SOVs with conventional pointwise velocimetry instrumentation. Despite the lack of empirical or observational evidence to confirm their existence and understand their dynamic behaviour, SOVs are nevertheless considered important drivers of mixing and sediment transport processes at confluences. Their causal mechanisms are also not fully understood, hindering progress towards a robust conceptual model of confluence turbulent mixing. To address these gaps, we present and analyse direct observations of highly dynamic and coherent SOVs captured in aerial drone video at a mesoscale confluence presenting a stark turbidity contrast between its tributaries. Eddy-resolved modelling demonstrates the dynamics of the SOVs can only be reproduced when a small density difference ($\Delta\rho$) is imposed between the tributaries ($\Delta\rho = 0.5$ kg/m^3). Our results conclusively demonstrate that SOVs do exist and that a small difference in density between the tributaries inverts the sense of rotation of the SOVs and their vertical position within the water column, causing important effects on the confluence's turbulent mixing regime.

Aerial observations and numerical simulations confirm density-driven streamwise vortices at a river confluence

J. Duguay[1], P. M. Biron[1], J. Lacey[2]

[1]Department of Geography, Planning and Environment, 1455 De Maisonneuve Blvd. W., Montreal, QC, Canada

[2]Department of Civil Engineering, Université de Sherbrooke, 2500 boul. de l'Université, Sherbrooke, QC, Canada

Key Points:

- Aerial views of turbidity gradients reveal streamwise orientated vortices (SOVs) at a mesoscale confluence
- modeling demonstrates the SOVs form due to a small density gradient between the tributaries
- The observed SOVs are spatially distinct from large-scale helical motion at the confluence

Corresponding author: J. Duguay, j_dug@live.concordia.ca

Abstract

When rivers collide, complex three-dimensional coherent flow structures are generated along the confluence's mixing interface. These structures play important roles in mixing streamborne pollutants and suspended sediment and have considerable bearing on the morphology and habitat quality of the postconfluent reach. A particular structure of interest - streamwise orientated vortices (SOVs) - were first detected in numerical simulations to form in pairs, one on each side of the mixing interface rotating in the opposite sense of the other. Since, it has proven difficult to detect SOVs in situ with conventional pointwise velocimetry instrumentation. Despite the lack of clear evidence to confirm their existence, SOVs are nevertheless considered important drivers of mixing and sediment transport processes at confluences. Additionally, their causal mechanisms are also not fully known which hinders a complete conceptual understanding of these processes. To address these gaps, we analyze observations of strongly coherent SOVs filmed in aerial drone video of a mesoscale confluence with a stark turbidity contrast between its tributaries. Eddy-resolved modeling demonstrates the SOVs' dynamics could only be accurately reproduced when a density difference ($\Delta\rho$) was imposed between the tributaries ($\Delta\rho = 0.5$ kg/m^3) – providing compelling evidence the observed SOVs are indeed a density-driven class of SOV. This work confirms that SOVs exist, expands understanding of their generative processes and highlights the important role of small density gradients (e.g., ≤ 0.5 kg/m^3) on river confluence hydrodynamics.

Plain Language Summary

Where rivers collide turbulent mixing of suspended sediments and pollutants affects the morphology and habitat quality of the reach downstream of the confluence. Streamwise orientated vortices (SOVs), resembling atmospheric tornadoes rotating parallel to the confluence's bed, were first predicted in computational fluid simulations in the early 2010s. Since, SOVs have garnered much interest, yet have evaded detection with conventional field instrumentation. Consequently, clear evidence of SOVs at river confluences has not been reported – leading to much debate on their existence and the fluid motions responsible for their formation. To advance these research aims, we present and analyze aerial observations of SOVs revealed at the confluence of two rivers with a strong contrast in turbidity. The simulations demonstrate the SOVs could only be accurately reproduced when a small difference in water density ($\Delta\rho$) was imposed between the rivers ($\Delta\rho = 0.5$ kg/m^3). Such differences commonly arise due to small gradients in the temperature and suspended sediment loads of the joining rivers. Our work confirms SOVs do exist and presents compelling evidence the observed SOVs are a novel density-driven class of SOV.

1 Introduction

The hydrodynamics of river confluences is a fascinatingly complex subject having attracted the attention of inquisitive minds for centuries (da Vinci L., 2009). The coherent flow structures generated within the confluence are key drivers of mixing and sediment transport processes. The roles of shear-induced vertically orientated Kelvin-Helmholtz (KH) instabilities (Rogers & Moser, 1992; De Serres et al., 1999; Rhoads & Sukhodolov, 2001; Constantinescu et al., 2016; Lewis & Rhoads, 2018; Biron et al., 2019) and helical cells caused by planform curvature on mixing at confluences have been studied extensively (Mosley, 1976; Rhoads & Kenworthy, 1995, 1999; Sukhodolov & Rhoads, 2001; Riley et al., 2015; Lewis & Rhoads, 2015; Rhoads & Johnson, 2018). While vertically orientated KH instabilities can be directly observed as swirls of debris or turbidity gradients on a confluence's surface (De Serres et al., 1999; Lewis & Rhoads, 2015; Biron et al., 2019; Duguay et al., 2022), helical cells are apparent only on cross-sections of the mean flow measured using acoustic velocimetry (Rhoads & Sukhodolov, 2001; Riley et al., 2015; Rhoads & Johnson, 2018; Yuan et al., 2021). Recently, episodic pulses in the confluence's mixing interface have been identified with large-scale particle image velocimetry (LSPIV) (Sabrina et al., 2021), a discovery highlighting the advantage of spatially resolved instantaneous measurement techniques to the study of confluence hydrodynamics. Though the causal mechanism of the pulses is not fully understood, they are likely due to unsteadiness in the water-surface pressure-gradient field as the flows compete for space within the confluence (Sabrina et al., 2021). Unlike KH instabilities, helical cells and episodic pulses, a fourth form of coherent flow structure - streamwise orientated vortices (SOVs) – have been suggested to exist yet have eluded detection in situ.

Streamwise orientated vortices were first predicted in eddy-resolved numerical modeling of a small-scale, asymmetrical concordant bed confluence (Constantinescu et al., 2011, 2012, 2016). The SOVs developed as back-to-back counter-rotating vortices, one flanking each side of the mixing interface, each rotating in the opposite sense of the other. Recent eddy-resolved modeling has also predicted single-sided SOVs (Duguay et al., 2022) or has failed to detect SOVs entirely (Guillén Ludeña et al., 2017; Cheng & Constantinescu, 2020), suggesting they need not form in the dual back-to-back model discussed by Constantinescu et al. (2011), nor are they universal to all confluences. SOVs are thought to arise from a downwelling of superelevated flow mechanism: as the opposing flows collide near the apex, a portion of their kinetic energy is converted to potential energy (i.e., superelevated surface), which subsequently reverts to kinetic energy as the superelevated mass is accelerated towards the bed (Constantinescu et al., 2011; Sukhodolov & Sukhodolova, 2019; Horna-Munoz et al., 2020). Though the numerical simulations of Constantinescu et al. (Constantinescu et al., 2011, 2012; Constantinescu, 2014; Constantinescu et al., 2016) indicate SOVs can develop at confluences, these studies could not clearly dissociate the SOVs from the large-scale curvature driven helical motion which often develops at confluences.

Recent field experiments at an in-stream field-scale confluences provide evidence of back-to-back counter-rotating SOVs on cross-sections of mean acoustic Doppler velocimetry (ADV) data (Sukhodolov & Sukhodolova, 2019). Though these measurements hint that SOVs are indeed spatially distinct from the larger-scale helical cells present, ultimately the authors concluded that "... separation of the SOV cells from the helical flow was not possible because of the coarseness of the measuring [ADV] grid" (Sukhodolov and Sukhodolova (2019), p. 608). Furthermore, the methods applied in Sukhodolov and Sukhodolova (2019) were unable to provide spatiotemporal details of the SOVs' dynamics, in particular, the possible bi-modal oscillations discussed in numerical studies (Constantinescu et al., 2011, 2012, 2016; Horna-Munoz et al., 2020). The work of Sukhodolov and Sukhodolova (2019) associates the causal mechanism of SOVs with local superelevation effects, yet how these effects differ from the curvature induced centrifugal superelevation driving large-scale helical motions is not entirely clear.

To complicate matters further, other sources of coherent streamwise orientated vorticity have also been identified at confluences. Studies have cited flow separation over the scour hole's avalanche faces as an important generator of streamwise vorticity (Best, 1988; Best & Roy, 1991; Biron & Lane, 2008; Duguay et al., 2022) and most recently, buoyancy effects caused by density gradients ($\Delta\rho$) between the incoming flows have been noted to vertically stratify the mixing interface through a "lock-exchange-like" mechanism, which invariably alters SOV production (Cheng & Constantinescu, 2020; Horna-Munoz et al., 2020; van Rooijen et al., 2020), though to what extent still remains uncertain. Thus, it is largely unclear how superelevation, flow separation and density effects interact to alter coherent streamwise vorticity in a confluence's mixing interface.

There is therefore little consensus on the existence of SOVs, their causal mechanisms and the extent to which they contribute to confluence mixing. Ideally, these topics could be addressed through spatiotemporally resolved empirical measurements, however, such measurements are difficult or impossible to obtain in situ due to the current limitations of acoustic velocimetry instrumentation. Direct observation of SOVs is an attractive alternative, though such observations also come with challenges. Inherently a feature of the subsurface flow, SOVs are difficult to visualise: the joining rivers often lack a turbidity contrast, rendering the SOVs "invisible" in aerial views, or when a sufficient turbidity gradient is present, waves and glare can occlude views of the subsurface turbulent billows (i.e., see supplementary videos Duguay et al. (2022)). Therefore, unlike KH instabilities, helical cells and episodic pulses, technological limitations and practical constraints have largely limited our understanding of SOVs to that which can be learned from eddy-resolved numerical modeling.

The variety of mixing patterns observed in the postconfluent reaches of natural confluences (Lane et al., 2008; Biron et al., 2019; Sukhodolov & Sukhodolova, 2019; Horna-Munoz et al., 2020; Duguay et al., 2022) is largely attributed to the complex and little understood interactions of the four mentioned forms of coherent flow structures (KH instabilities, helical cells, episodic pulses and SOVs). Therefore, a deeper understanding of SOVs, with a specific focus on their causal mechanisms and interactions with other coherent flow structures is necessary if a robust conceptual model of confluence hydrodynamics is to be obtained. To advance this aim, herein we analyse full-scale aerial observations of SOVs and their dynamic coupling to episodic pulses at a mesoscale confluence characterised by an abrupt contrast in turbidity between the incoming flows. Eddy-resolved modeling compliments the observations, providing convincing evidence that buoyancy effects resulting from weak density gradients ($\leq$ 0.5 kg/m^3) between the incoming rivers are responsible for developing this density-driven class of SOV.

2 Methods

2.1 Field site and measurements

The field site is located at the confluence of the Coaticook (tributary) and Massawippi (main) rivers near Sherbrooke, Quebec, Canada (Fig. 1). At discharges of $Q > 15$ m^3/s, the Coaticook, located in an agricultural watershed (514 km^2), usually contains a high concentration of suspended sediment (e.g., > 200 mg/l). In contrast, the Massawippi, which flows from Lake Massawippi (watershed area of 610 km^2) through a mostly wooded portion of its watershed for approximately 9.6 km, is generally much less turbid and often clear. The resulting turbidity contrast between the two rivers makes the site ideal to observe coherent flow structures in aerial video. Though evidence of SOVs is often visible in aerial drone videos of the confluence's mixing interface (and SOVs are often likely present even if not visible), the conditions necessary for such clear visual observations as those presented in our study rarely occur (likely every 2 to 4 years based on the principal author's personal observations at the confluence) and when they do, these clear observations are generally fleeting (lasting only a few hours before the flow rates significantly change). These factors, combined with the practical constraints of working in depths of up to 2 m in swift currents, make their detailed study with conventional acoustic velocimetry methods extremely difficult in situ. However, because of the clarity of the SOVs discussed herein, much can be learned of this elusive form of coherent flow structure through analysis of aerial video.

Discharges are measured continuously every 15 minutes in both tributaries at gauging stations located 2.5 km and 8 km upstream in the Coaticook and Massawippi respectively. There are no major tributaries between the gauging stations and the confluence, and the watershed areas downstream of the gauging stations represent 1.1% and 3.0% of the total watershed areas for the Coaticook and Massawippi respectively. Therefore, the gauged discharges are considered representative of the relative magnitudes of the incoming flows. The junction angle is 120 °, with a sharp meander in the Coaticook River upstream from the confluence (Fig. 1). The bathymetry of the confluence was measured in the summer of 2020 using a mobile differential geographical positioning system (Fig. 1c). Grain size distributions on the Massawippi side of the confluence were measured in the fall of 2020 using the Wolman method (Wolman, 1954). Median diameter (D_{50}) is 75 mm on the Massawippi side. Grain sizes on the bed of the Coaticook are fine to coarse sand (0.125 mm to 1 mm). Dunes have been observed near the inner bank in the upstream reach of the Coaticook.

A deep scour hole extends ≈ 33 m upstream and ≈ 31 m downstream of the apex on the Coaticook side (Fig. 1c). The scour upstream of the apex, and to a large extent, downstream of the apex is caused by meander bend secondary flow (Blanckaert & de Vriend, 2004). The bathymetry fits the conceptual description of a confluent meander bend (Riley et al., 2015), however at this confluence, the main river (the Massawippi by watershed area) unusually

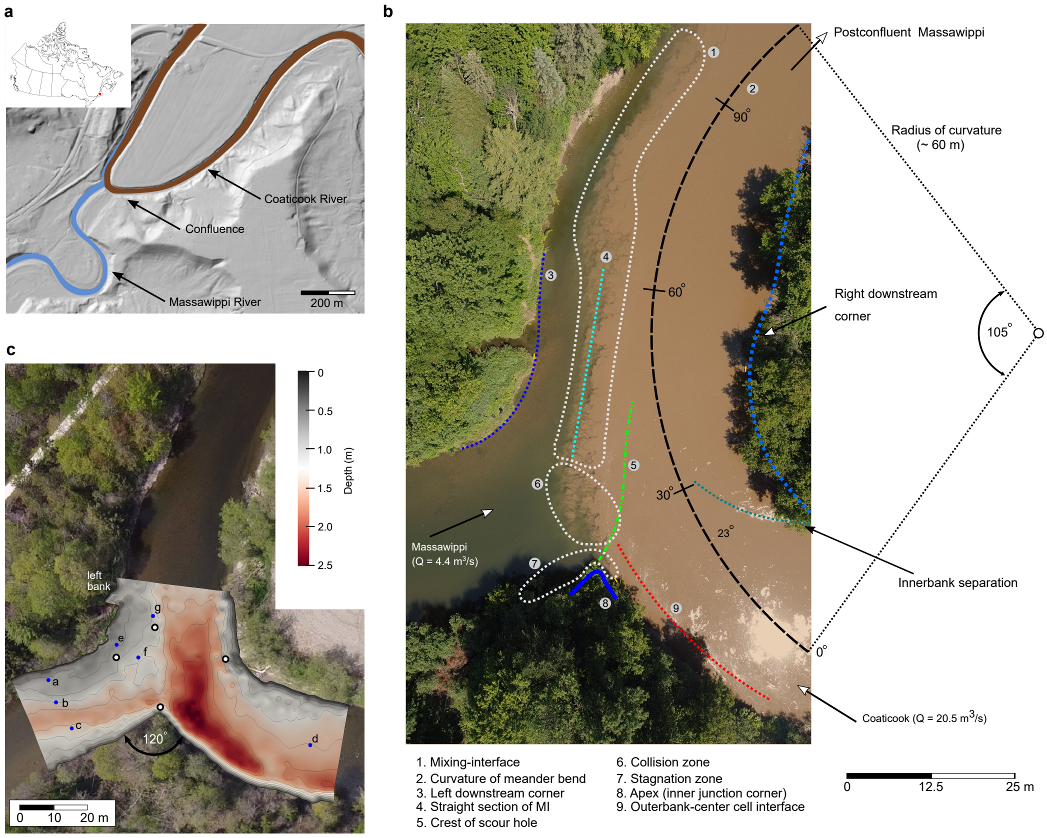

Figure 1. Massawippi-Coaticook meander-bend confluence. **a**, High-elevation planform geometry of the confluence located in the province of Quebec, Canada (45°18'50"N 71°53'55"W). At high discharge, the Coaticook, which flows through an agricultural watershed is generally turbid. The Massawippi, flowing through a forested watershed is often clear. **b**, Planform characteristics and hydrodynamic zones on a high elevation view of the confluence taken at 15:41:00 UTC on July 9th, 2020. **c**, Bathymetry of the confluence colored by depth below the free surface (146.07 m above sea level) during the numerical model validation field campaign of October 22nd, 2020. Water surface elevation was 0.07 m higher on July 9th (146.14 m above sea level) than on October 22nd, 2020. Contoured region delimits extents of the numerical modeling domain. Black contoured circles indicate locations of the four ground reference points for large-scale particle image velocimetry measurements of October 22nd, 2020. Locations of propeller current meter profiles are indicated with blue dots (a-g).

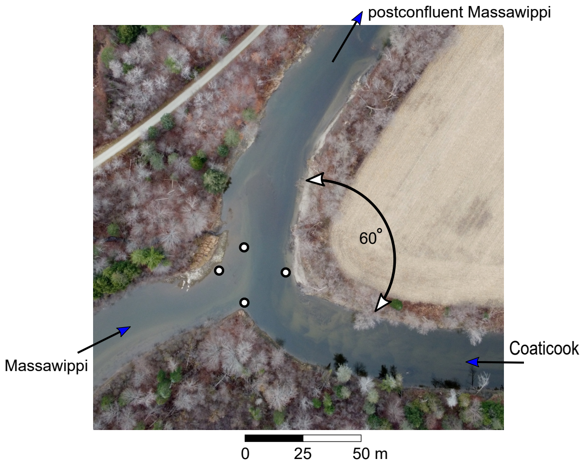

Figure 2. High elevation view of confluence planform. Aerial view of the Coaticook-Massawippi confluence on November 15^{th}, 2020 under clear-water conditions taken approximately 200 m above the confluence. Image included to emphasis the meander-like bend the Coaticook makes as it joins the post-confluent channel. Dune formations visible upstream of the apex in the Coaticook.

joins the curving tributary (Coaticook). The scour zone on the Coaticook side shifts toward the inner bank of the bend as the Massawippi deposits its bedload, forming a bar in what would normally be a meander bend "outer bank" scour zone. Figure 2 illustrates this in a high-elevation aerial view of the confluence under clear water conditions.

Drone imagery was collected on July 9^{th}, 2020 when a sharp contrast in turbidity between the (turbid) Coaticook and (clear) Massawippi allowed for clear identification of coherent flow structures in the mixing zone (see Video 1). Important hydraulic parameters of the confluence during the aerial observations are presented in Table 1 (see notes for additional details). On July 9^{th}, 2020, only the drone video and the water surface level were recorded. Mean cross-sectional velocities were calculated based on discharges obtained from the gauging stations and the cross-sectional areas obtained from the bathymetry and measured water surface level. A description of the confluence's predominant flow patterns inferred from aerial drone video on July 9^{th}, 2020 is available in Supplementary Materials.

2.2 Numerical model

A hydrodynamic numerical model of the Coaticook-Massawippi confluence was constructed to investigate the causal mechanism of the SOVs observed on July 9^{th}, 2020. In

Table 1. Hydraulic conditions during SOV observations on July 9^{th} and numerical model validation data collection on October 22^{nd}, 2020

Date	boundary	Q	B	A	h_{max}	ρ*	H	U_{av}	**Fr**	**Re**
July 9^{th}, 2020 - $M_r = 16.9$										
	Massawippi	4.4	29.1	34.4	1.60	996.92	1.19	0.13	0.04	153400
	Coaticook	20.5	29.2	44	1.91	997.42	1.50	0.47	0.12	700300
	outlet	24.9	33.8	39.3	1.42		1.02	0.63	0.19	730800
Oct. 22^{nd}, 2020 - $M_r = 0.91$										
	Massawippi	13.02	29.1	32.5	1.54	-	1.12	0.40	0.12	448000
	Coaticook	13.92	29.2	41.5	1.99	-	1.43	0.34	0.09	486200
	outlet	26.94	33.8	37.1	1.38		0.95	0.73	0.24	693500

Notes: Values derived from discharges measured at the gauging stations, water surface levels measured during the observations and bathymetric data gathered in the summer of 2020. Values pertain to the inlet and outlet cross-sections of the numerical model's simulated domain. Q discharge (m^3/s), B width (m), A wetted area (m^2), h_{max} maximum depth (m), ρ* estimated density (see subsection River densities and simulated cases), H average cross-sectional depth (m), U$_{av}$ average cross-sectional velocity (m/s), **Fr** is the Froude number ($\mathbf{Fr} = U_{av}/\sqrt{gH}$), **Re** is the Reynolds number ($\mathbf{Re} = HU_{av}/\nu$). Momentum ratio, $M_r = \rho_C Q_C U_{av}^C / \rho_M Q_M U_{av}^M$ (subscript $_C$ for Coatiook, $_M$ for Massawippi).

the model, the incompressible continuity (Eq. 1) and Navier-Stokes (Eq. 2) equations (in Cartesian coordinates) are solved using a large-eddy simulation (LES) approach with OpenFOAM's (v2012) *twoLiquidMixingFoam* solver. OpenFOAM is an open-sourced computational fluid dynamics code based on the finite volume method (Weller et al., 1998). The *twoLiquidMixingFoam* solver has been extensively validated for simulating buoyancy driven mixing of two fluids of different density (Gruber et al., 2011; Lai et al., 2015; Zhang et al., 2016; Grbčič et al., 2019). In Eqs. 1 and 2 the spatial vector is defined as $x_i \equiv x_1, x_2, x_3$ indicating, respectively the longitudinal (x), lateral (y) and vertical (z) axes. The velocity vector is defined as $u_i \equiv u_1, u_2, u_3$ indicating components along the longitudinal (u), lateral (v) and vertical (w) axes. Time, pressure, kinematic viscosity and the constant of gravitational acceleration are indicated respectively by t, p, ν and g.

$$\frac{\partial u_i}{\partial x_i} = 0 \tag{1}$$

$$\frac{\partial \overline{u_i}}{\partial t} + \frac{\partial \overline{u_i u_j}}{\partial x_j} = -\frac{1}{\rho}\frac{\partial \overline{p}}{\partial x_i} + \frac{\partial}{\partial x_j}(\nu \frac{\partial \overline{u_i}}{\partial x_j}) - \frac{\partial \tau_{ij}^{SGS}}{\partial x_j} + \rho g \tag{2}$$

In a LES, the spatial filtering process results in subgrid stress terms (τ_{ij}^{SGS}, (Saguat, 2001)) in the momentum equations (Eq. 2) for which the Smagorinsky subgrid scale model (Eq. 3) has been used as closure (Smagorinsky, 1963).

$$\tau_{ij}^{SGS} = \overline{u_i u_j} - \bar{u}_i \bar{u}_j = \frac{2}{3}\tau_{kk}\delta_{ij} - 2\nu_{SGS} dev(\overline{S_{ij}}) \tag{3}$$

The subgrid stress terms are calculated with Eq. 3, which invokes the resolved rate of strain tensor ($\overline{S_{ij}}$, Eq. 4) and the subgrid scale turbulent viscosity (ν_{SGS}, Eq. 5). In Eq. 5 a filter length Δ based on cell volume (V_c) is used ($\Delta = c(V_c)^{1/3}$), where c is a constant equal to 1 and V_c is the cell volume) and the Smagorinsky constant (C_k) is 0.094. In near wall regions the standard Van Driest damping function is applied to let $v_{SGS} \rightarrow 0$.

$$\overline{S_{ij}} = \frac{1}{2}\left(\frac{\partial \overline{u_i}}{\partial x_j} + \frac{\partial \overline{u_j}}{\partial x_i}\right) \tag{4}$$

$$\nu_{SGS} = C_k \Delta k_{SGS}^{0.5} \tag{5}$$

The *twoLiquidMixingFoam* solver uses a fluid fraction method (α) to determine ρ resulting from the mixing of two miscible fluids of different density. Flow of the Coaticook (subscript 1) is considered $\alpha = 1$ and that of the Massawippi $\alpha = 0$ (subscript 2). Practically, fractional values of α can be interpreted to indicate the fractional volume of fluid in each cell originating from the Coaticook. The spatiotemporal evolution of α is calculated using an advection-diffusion equation (Eq. 6, $\boldsymbol{u}$ velocity field, t time, D_{ab} molecular diffusivity between miscible fluids a and b ($D_{ab} = 10^{-6}$ m^2/s), S_c is the turbulent Schmidt number (S_c = 1)). The dynamic viscosity (μ) and density at each computational cell are determined as fluid fraction weighted averages using Eqs. 6, 7 and 8. Additional details of the numerical methods (i.e. finite-volume approach, the Smagorinsky SSG model, discretization schemes and solution methods) are extensively documented elsewhere (Pope, 2011; Moukalled et al., 2016). Specifics related to the numerical schemes applied in OpenFOAM are available in Supplementary Materials.

$$\frac{\partial \alpha}{\partial t} + \nabla \cdot (\mathbf{u}\alpha) = \nabla \cdot \left(\left(D_{ab} + \frac{\nu_t}{S_c} \right) \nabla \alpha \right) \tag{6}$$

$$\rho = \rho_1 \alpha + \rho_2 (1 - \alpha) \tag{7}$$

$$\mu = \mu_1 \alpha + \mu_2 (1 - \alpha) \tag{8}$$

The high Reynolds numbers of the confluence and its large physical scale make wall-resolved large-eddy simulations computationally impractical. However, LES with wall functions curtails this requirement by allowing less mesh resolution near the wall (Keylock et al., 2012; Rodi et al., 2014). The wall modeled approach (WMLES) has been applied to successfully investigate large-scale turbulent phenomena within the outer region of the water column in fluvial applications (Van Balen et al., 2009; Schindfessel et al., 2015; Khosronejad, Flora, & Kang, 2020). A velocity-based wall function is applied to calculate the near-wall turbulent viscosity and bed shear stress induced by the rough solid boundary.

A fixed time-step of 0.005 s maintained the average Courant-Friedrich number at 0.2 and the maximum below 0.8. Simulations were performed on Compute Canada's high-powered computing clusters. The domain was decomposed and solved on 160 processors (Intel Gold 6148 Skylake with clock frequencies of 2.4 GHz) and took $\approx$ 24 hours to simulate 100 s of flow.

2.2.1 Computational domain

The computational domain of the confluence was constructed in the following steps. First, sparse (1-3 m separation) points taken with a differential ground positioning system were measured at the confluence in the summer of 2020. These points were interpolated to a regularly spaced grid (0.25 m) using a thin plate spline algorithm (QGIS 3.14.1-Pi). A screened Poisson surface reconstruction (Meshlab software) was performed on the interpolated points to generate a 3D stereolithography geometry. The geometry was imported into the mesh generation software Pointwise (V18.3R2) to produce the predominantly tetrahedral unstructured mesh for the computational domain. Upstream of the confluence's apex, $\approx$ 30 and 50 m long reaches of the Massawippi and Coaticook were included to permit planform induced secondary flow to develop. The near-wall cell height was fixed at 0.015 m and expanded over $\approx$ 10 vertical layers with an expansion factor of 1.2 to an average edge length of 0.08 m in the mixing interface and 0.12 m elsewhere. An additional 10-20 cells extend from the edge of the near-wall layers to the free surface for a total of 20 to 30 vertical grid points in the mixing interface. Mesh density was increased in the mixing interface to permit a higher spatial resolution of the coherent turbulent structures of interest while maintaining a reasonable number of computational cells ($\approx$ 37 million). Because the turbulent length scales of interest occur between 0.5 m to 6 m in the mixing interface, the 0.08 m edge length resolution of the mesh within the mixing interface permits the most energetic turbulent structures to be resolved by $>$ 7 cells in each direction, respecting guidelines proposed by (Keylock et al., 2012). Also, an index of mesh resolution quality study following the procedure outlined by Celik et al. (2005) was performed and used to confirm adequate spatial resolution of the domain's spatial resolution within the mixing interface. Our mesh resolution is comparable to that adopted in other contemporary eddy-resolved numerical models of confluence hydrodynamics (Constantinescu et al., 2012, 2016; Cheng & Constantinescu, 2020; Horna-Munoz et al., 2020).

2.2.2 Boundaries

Fully developed flow profiles containing spatiotemporally coherent vortices were applied at the inlets of the main domain using a two-step precursor simulation process. First, cross-sectional profiles calculated using two-equation k-ω RANS precursor simulations were obtained on short meshes extruded along the outward normal of each inlet boundary. Cyclic boundaries were applied at the inlet and outlet of these precursor simulations and discharge was induced with a momentum source term. A no-slip condition was applied to the bed and a free-slip (symmetry) boundary was applied at the free surface. Converged profiles at the outlet of the precursor simulations were supplied to the divergence-free synthetic eddy generation boundary condition (DFSEM) (Poletto et al., 2013) to introduce spatiotemporally coherent turbulent structures into the main computational domain during runtime. The interested reader can find OpenFOAM specifics related to the boundaries of the simulation in Supplementary Information.

In the main simulation, a zero-flux Neumann boundary condition was applied for all vector and scalar fields at the outlet. A no-slip boundary condition was used for the velocity at the confluence's bed (wall). A velocity-based wall function was implemented to provide estimates of the near-wall turbulent viscosity. A free-slip (symmetry) boundary was applied to the free surface to ensure zero flux across the boundary and free-slip lateral and streamwise components over the horizontal free surface. Other studies have successfully applied this approach to model short reaches presenting minimal free-surface deformation (Van Balen et al., 2009; Constantinescu et al., 2011; Kara et al., 2015; Schindfessel et al., 2015; Le et al., 2019). The low Froude numbers characteristic of the confluence (< 0.3, Table 1) suggest free-surface deformations are expected to be minimal (Khosronejad et al., 2019; Khosronejad, Arabi, et al., 2020), which was visually confirmed on July 9^{th}, 2020 and on October 22^{nd}, 2020 (date of field data validation collection).

2.2.3 River densities and simulated cases

The SOV observations of July 9^{th}, 2020 were unexpected and unplanned as this field visit was intended to perform routine water surface elevation measurements and aerial drone video of the mixing interface. Such outings were carried out because of previous (yet much less convincing) sightings of secondary flow structures at the confluence when the discharge of the Coaticook was over 10 m^3/s. On July 9^{th} 2020, the importance of density gradients in the formation of the SOVs had not yet occurred to the authors and consequently neither had the importance of temperature and suspended sediment gradients, which is why we were not equipped to obtain such data on this date. It was not until preliminary numerical results were obtained in early 2021 that the importance of $\Delta\rho$ in the formation of the SOVs was realized. Afterward, communications with the operator of the gauging stations allowed the temperature of the Massawippi at the time of observation (25.5 °C) to be obtained, but water temperatures at the Coaticook's gauging station were not available. However, shortly after the drone flight of July 9^{th}, the principal author waded into the mixing interface and could distinctly feel the passage of the cool billows of the turbid Coaticook within the SOV, a difference conservatively estimated to be approximately 1.5 °C. A subsequent visit to the mixing interface at lower flow rates, yet with a thermometer (OMEGA HH-

25KC thermometer) confirmed such small differences in temperature can indeed be readily detected with the hand.

If the temperature of the Coaticook is considered to be 24 °C, the cooler Coaticook is estimated to be 0.38 kg/m^3 denser than the warmer Massawippi (ρ_C = 997.29 kg/m^3 Coaticook at 24 °C, ρ_M = 996.92 kg/m^3 Massawippi at 25.5 °C). The densities of the tributaries were calculated as,

$$\begin{aligned}\rho &= 999.83952 + 16.945176t - 7.9870401 \cdot 10^{-3}t^2 \\ &\quad -46.170461 \cdot 10^{-6}t^3 + 105.56302 \cdot 10^{-9}t^4 \\ &\quad -280.54253 \cdot 10^{-12}t^5)/(1 + 16.897850 \cdot 10^{-3}t) \qquad (9)\end{aligned}$$

where ρ indicates density in kg/m^3 and t the temperature of the water in °C (Jones & Harris, 1992). Suspended sediment concentration (SSC) in the Coaticook, estimated at 0.20 kg/m^3 based on SSC measurements taken during subsequent outings during the 2021 season, would increase ρ_C by 0.12 kg/m^3, whilst the clarity of the Massawippi suggests SSC should have a negligible impact on its density. Therefore, a difference in density ($\Delta\rho$) of 0.50 kg/m^3 between the Coaticook and Massawippi is deemed a reasonable estimate for the July 9th conditions.

We present results from two simulations: one in which the densities of the Coaticook and Massawippi are equal denoted as $\Delta\rho_{0.0}$ and one where the Coaticook is 0.5 kg/m^3 denser than the Massawippi, denoted as $\Delta\rho_{0.5}$. Exploratory simulations varying $\Delta\rho$ between 0.0 and 3.0 kg/m^3 were also performed, however, only $\Delta\rho_{0.5}$ was retained for further analysis in this study because of its accurate predictions of the coherent flow structures in the mixing interface and because it is a physically plausible value of $\Delta\rho$ based on SSC and temperature measurements taken at the confluence at several occasions in the following field season of 2021. Simulations with higher magnitudes of $\Delta\rho$ still produced SOVs, however, the front of dense Coaticook extended farther towards the left bank of the confluence and the SOVs had larger widths. Therefore larger-scale density effects were observed in these models with an increasing magnitude of $\Delta\rho$. A $\Delta\rho$ magnitude of 0.5 kg/m^3 in contrast, was able to produce near-circular SOVs similar to those observed in the aerial drone video. The interesting effects of larger magnitudes of $\Delta\rho$ on secondary flow structure at the confluence are the focus of ongoing research.

2.2.4 Numerical stationarity analysis and data acquisition

The flow field from the final time-step of a long duration (2000 s) coarse grid simulation ($\approx$ 9 million cells) of each case ($\Delta\rho_{0.0}$ and $\Delta\rho_{0.5}$) was mapped to the fine (37 million cells) mesh for use as initial conditions. The fine mesh cases were then run for 1000 s before recording data for analysis. This 1000 s spin-up period ensured flow field artifacts from the initial conditions had sufficient time to exit the domain (required $<$ 200 s) and that the instantaneous flow field was in a stationary regime before data recording. Considering the average cross-sectional velocity of 0.63 m/s at the outlet and a domain length of $\approx$ 65 m, the spin-up period equates to $\approx$ 10 flow-through periods. Statistical stationarity was assessed by performing an Augmented Dickey-Fuller (ADF) unit test on velocity time-series at various locations throughout the domain for the final 800 s of the spin-up period. ADF statistics indicated the absence of long-duration trends (ADF statistics $p < 0.001$). Furthermore, first and second-order turbulent statistics of 10 randomly selected 300 s segments extracted from the retained 800 s period also closely approximated the global values acquired over the 800 s period. After the 1000 s spin-up period, the simulations were run for an additional 600 s, over which temporally averaged quantities were measured for analysis. Instantaneous results were recorded every 2 s during the final 400 s.

2.3 Large-scale particle image velocimetry

Drone videos of the confluence on October 22^{nd}, 2020 were taken $\approx$ 30 m above the water surface to perform large-scale particle image velocimetry (LSPIV) for numerical model validation purposes (see section 3). A Mavic Mini (model MT1SS5) captured video at 30 fps video at 2720 x 1530 resolution. The drone's camera is fitted on a 3-axis gimbal (tilt, roll, pitch), which greatly reduced instabilities in the video. Video frames were stabilized and orthorectified using four ground reference points (GRPs) (see Fig. 1c) following the process described below. The buoyant GRPs, with a black outside annulus 0.45 m in diameter and a central fluorescent orange interior 0.3 m in diameter, were centered over steel bars driven into the riverbed, allowing the GRPs to freely displace vertically on the surface yet restrict lateral movements to $\pm$ 0.02 cm. The black annulus improved the automatic detection of the white central disk in the video frames.

The orthorectification procedure adjusts individual frames so the central pixels of each GRP coincides with its stabilized coordinate, determined as the location of the GRP in the first frame of the video, corrected to adhere to a constant scaling factor (meters per pixel). Pixels are assumed to lie on a horizontal plane (i.e. the water's surface). The scaling factor is determined as the average of the real-world distance of the lines connecting the GRPs divided by the average pixel distances of these lines in the first frame of the video. The process is performed in 3 steps: (1) extraction of the individual frames, (2) automated detection of the centres of the four GRPs in each frame, and, (3) application of a perspective transformation to the frames to adjust the pixel coordinates of the GRPs to their corrected locations (using OpenCV's *getPerspectiveTransform* and *warpPerspective* functions). This processing was done using a Python code *pyRiverDrone* developed in-house.

For the LSPIV experiments, light-colored wood chips $\approx$ 1.5 cm in diameter were used as seeding. Seeding the entire surface of the confluence simultaneously was not possible at this mesoscale confluence. Instead, each tributary was seeded at closely separated times ($<$ 10 mins between seeding events) at three different lateral positions. Seeding locations were chosen near the left and right banks and the center of each channel. Seeding was dispersed from a small watercraft attached to fixed lines $\approx$ 23 m and 47 m upstream of the confluence apex in the Massawippi and Coaticook respectively. Drone videos of each of the seeding events were carried out for 120 seconds. The drone videos were down sampled from 30 frames-per-second (FPS) to 5 FPS and orthorectified using the procedure described above. Vector processing was done in LaVision's DaVis particle image velocimetry software version 8.3.1. A double pass 64 x 64 px, 50 % overlap time-series cross-correlation was performed. A median 2 standard deviation vector removal and replacement filter were applied on the intermittent and final vector fields. The spatial resolution of the vector fields obtained from each video was 32 pixels, or $\approx$ 0.48 m. The mean vector fields obtained from each video were amalgamated into a single vector field representing an estimate of the surficial velocity distribution over a $\approx$ 730 m^2 region of the confluence's flow field (Fig. 3).

3 October 22nd, 2020 numerical model validation

The numerical modeling approach was validated after the July 9th, 2020 observations with field measurements obtained on October 22nd, 2020. Numerical results for the conditions present on October 22nd, 2020 were compared to mean large-scale particle image velocimetry (LSPIV) measurements and velocity profiles sampled at 7 accessible locations using a propeller current profiler (locations marked in Fig. 1c). The hydraulic conditions on 22nd of October 2020 are presented in Table 1. Figure 3 compares numerical predictions of surficial mean velocity magnitude distributions ($\overline{U}_{uv}$) to those obtained using aerial particle image velocimetry. The model accurately predicts (1) the accelerating flow on the Massawippi side of the confluence, (2) the position of the mixing interface indicated by where the streamlines of the tributaries meet, (3) the accelerating flow over the downstream section of the Coaticook confluence, (4) the distribution of isocontours of mean surficial velocity magnitude (e.g. the white band for $\overline{U}_{uv}$ = 0.55 m/s in Fig. 3) and (5) the general agreement of the extent of the stagnation zone on the Coaticook side of the apex. The model also reproduces the sharp lateral velocity gradient across the mixing interface.

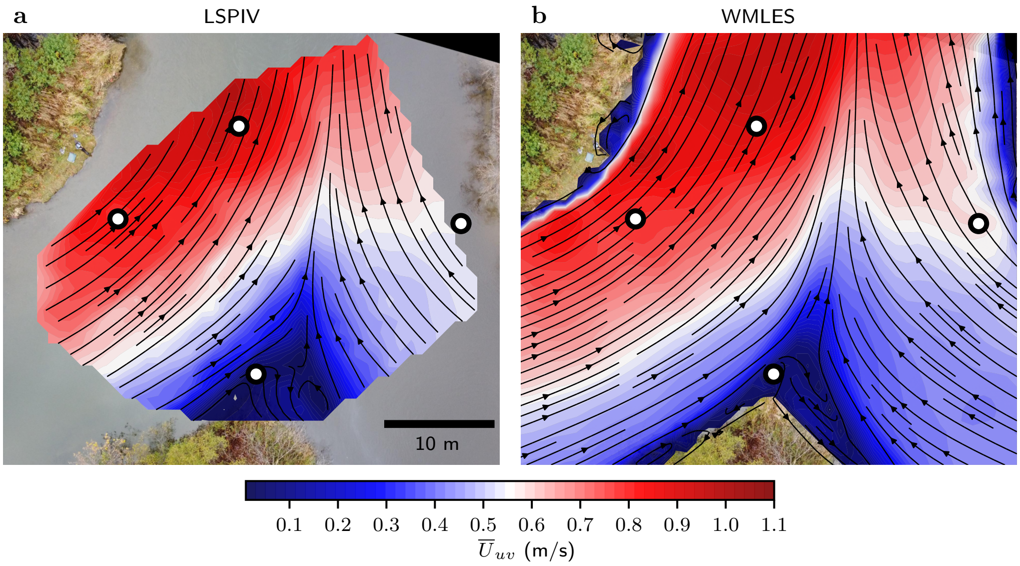

Figure 3. Mean surface velocity comparison of LSPIV and WMLES data. **a**, Surface distribution of $\overline{U}_{uv}$ with streamlines indicating mean flow direction obtained with large-scale particle image velocimetry on taken on October 22nd, 2020 (magnitude of mean streamwise and lateral velocity vector components). Contours delimit zone of valid vectors. **b**, Distribution of $\overline{U}_{uv}$ on the surface predicted by wall-modelled large-eddy simulation (WMLES).

Figure 4 compares predicted vertical profiles of mean velocity magnitude ($\overline{U}$) with their empirical counterparts measured using a propeller current meter (letters, Fig. 1c). The correspondence between measured and predicted profiles in the outer region of the flow supports the accuracy of the imposed inlet conditions (Figs. 4a,b,c,d) while the acceptable predictions in the wall-region ($z/h < 0.15$) attests to sufficient accuracy of the wall modeling and near-wall meshing approaches.

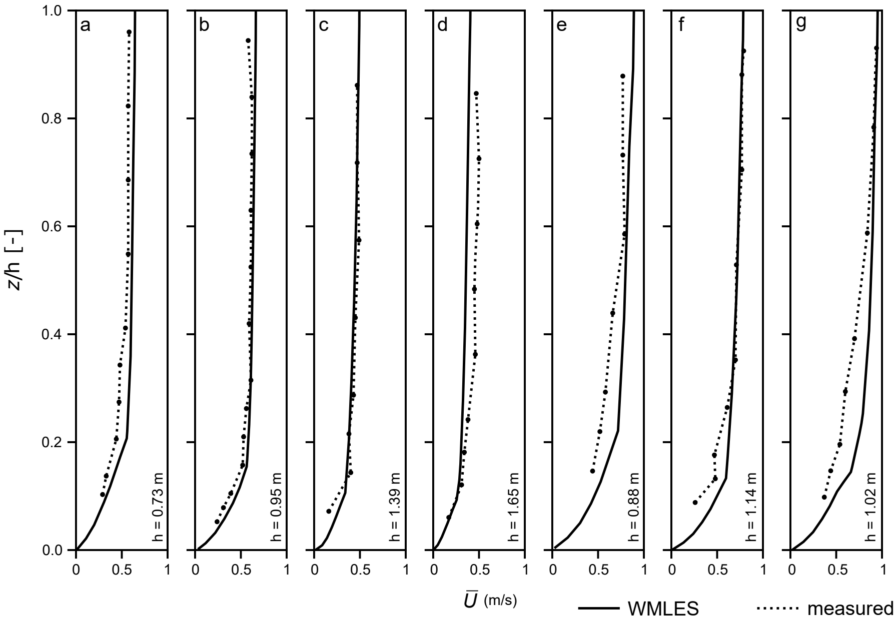

Figure 4. Comparison of numerical and measured velocity profiles over depth. a-f, Comparison of predicted (WMLES) vertical profiles of $\overline{U}$ to measured profiles obtained with a current meter at the 7 sampling locations (see Fig. 1c) on October 22^{nd}, 2020. z is the height above the bed and h is the depth at the sampling location.

The water surface on July 9^{th} was 0.07 m higher than on October 22^{nd}. Aside from the higher water surface, and different flow rates, all other modeling parameters of the October 22^{nd} simulation are identical to July 9^{th}. The correspondence between numerical and empirical results for the October 22^{nd} condition combined with the good agreement between observed and predicted coherent flow structures for the July 9^{th} conditions (see Results), supports the model's ability to provide insights into the hydrodynamics of the Coaticook-Massawippi confluence.

4 Results

4.1 Aerial observations of SOVs

Excellent views of SOVs displaying clear rotational motions were filmed with an aerial drone over a 500 s period on the 9^{th} of July 2020 (Video 1). Video 2 presents a 60 s clip of Video 1 (clip between 90 s and 150 s) at 1x playback and 8x playback speeds. The dynamic response of an exceptionally coherent rotating SOV to a passing episodic pulse is depicted in a time series of still images extracted from Video 2 in Fig. 5. Between 0 and 15 s in Video 2 (Figs. 5a-c), the subsurface turbid water on the Massawippi side of the partition line (line of sharpest turbidity gradient on the surface, see white dotted line in Fig. 5d) defining the advancing front of the episodic pulse is loosely coherent. Between 15 s and 22.5 s (Figs. 5c-d), a remarkably coherent primary SOV revolving clockwise around the streamwise axis (pointing downstream) takes form. As the front of the pulse advances farther, near-bed turbid water between the partition line and the right limit of the primary SOV upwells into the growing primary SOV (see Video 2). Simultaneously, a thin layer of clear Massawippi water flows above the primary SOV over much of the mixing interface. The thickness of this clear, overlying layer decreases with distance from the confluence apex resulting in a longitudinal, depth-induced color gradient over the visible portion of the SOV in Fig. 5d-f. Downstream of the collision zone (i.e. where the flows collide with maximum lateral momentum, Fig. 1b), the mixing interface becomes confined both laterally and vertically as flow accelerates over the shallow bathymetry into the postconfluent channel. Finally, the coherence of the primary SOV diminishes as the episodic pulse recedes (Fig. 5g-i).

The spatiotemporal coherence of the SOVs is evident in the space-time matrices presented in Fig. 6b. To construct Fig. 6b, 2 frames per second were extracted from Video 1, then gray-scaled pixel intensities within six rectangular zones straddling the centerline

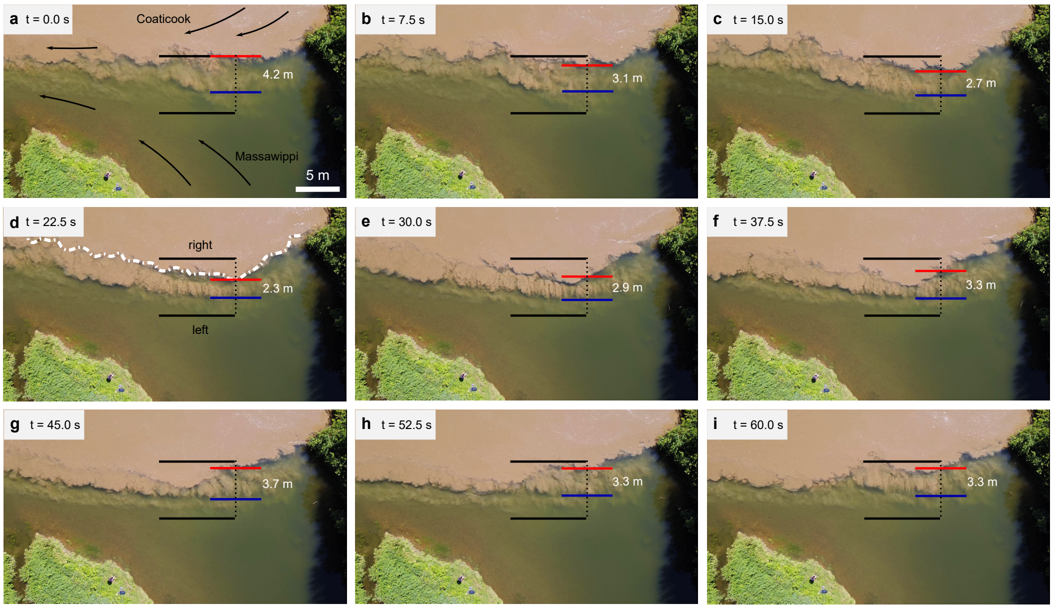

Figure 5. Life-cycle dynamics of the primary SOV. a-i Still images extracted at 7.5 s intervals from Video 2. *t* starts at the beginning of Video 2. The loosely coherent subsurface turbid waters of the Coaticook (**a**) are observed to rapidly cohere (**b**, **c**, **d**) as the episodic pulse advances to its farthest location (**e**) at ≈ 30 s into the cycle. As the pulse recedes, the coherence of the primary SOV diminishes (**g-i**). Black arrows (**a**) indicate the mean direction of incoming surface flows. Black bars are placed at fixed locations in each subplot to assist visualization of the lateral migration of the mixing interface with time. Red bars indicate the approximate lateral limit of the advancing partition line of the episodic pulse (sharp gradient on the surface between turbid and clear water, identified by a white dot-dashed line in **d**). Blue bars indicate the approximate left limit of the primary SOV. During the passage of this typical episodic pulse, the left-most limit of the primary SOV maintains approximately the same lateral position, despite the partition line translating left by upwards of 1.9 m.

streamwise axis of the mixing interface (Fig. 6a) were sampled from each frame. The dimensions of each sampling zone were respectively 12 m and 0.37 m in the lateral and streamwise directions and spaced longitudinally from one another by 4 m. The extracted matrices for each zone were averaged along their longitudinal axis (25 pixels equal to 0.37 m) to obtain a lateral line of average pixel intensities (perpendicular to the x axis in Fig. 6a). Chronologically ordering these lines for each x location for the 500 s duration of Video 1 produces one of the space-time matrices in Fig. 6b.

In Fig. 6b, deep billows of subsurface turbidity appear under clear Massawippi water at $x = 0$ m. Farther downstream, at $x = 8$ m, the turbid billows have formed into a primary SOV striated with lateral bands of clear water from the Massawippi (see yellow arrows Fig. 6b). A smaller secondary SOV appears adjacent to the primary SOV over the 500 s period. Evidence of a tertiary SOV is also observed farther downstream (e.g. $x = 16$ m, Fig. 6b). In Video 1, the primary, secondary, and tertiary SOVs all appear to have a clockwise sense of rotation. By $x = 4$ m the primary SOV begins to splay on the free-surface, identifiable as 'flattened' tops (red circles, Fig. 6b). The coherence of the primary SOV is strongest when the episodic pulses attain their maximum lateral displacement (e.g. between 90 s and 150 s, red opaque rectangular zone in Fig. 6b). Splaying becomes more accentuated over the shallower bathymetry near $x = 8$ m. Farther downstream the primary SOV is often occluded by the splayed near-surface water (e.g. $x >= 12$ m). The lateral scale of the primary SOV varies between 2 m ($0.06B$) and 4 m ($0.12B$), and the secondary SOV between 1 ($0.03B$) and 2 m ($0.06B$), whilst that of the tertiary SOV is approximately 0.5 m ($0.015B$). The maximum amplitude of the episodic pulses occurs at $x = 4$ m and is ≈ 4 m ($0.12B$) in width, with a period of ≈ 50 s (0.02 Hz). The non-linearity of the dotted lines joining the space-time locations of individual episodic pulses in Fig. 6c indicates streamwise acceleration of the flow within the mixing interface as it enters the postconfluent channel.

4.2 Eddy-resolved modeling

Near the confluence apex, the consistency with which the turbid billows from the Coaticook River appear underneath the clear surrounding Massawippi River suggests they are denser (Video 1, Fig. 5). Thus eddy-resolved numerical modeling accounting for a density difference ($\Delta\rho$) of 0.5 kg/m^3 between the Coaticook and Massawippi was conducted to provide insights on the hydrodynamics of the confluence and causal mechanisms of the observed SOVs. An equal density simulation ($\Delta\rho_{0.0}$) was also performed for comparative purposes.

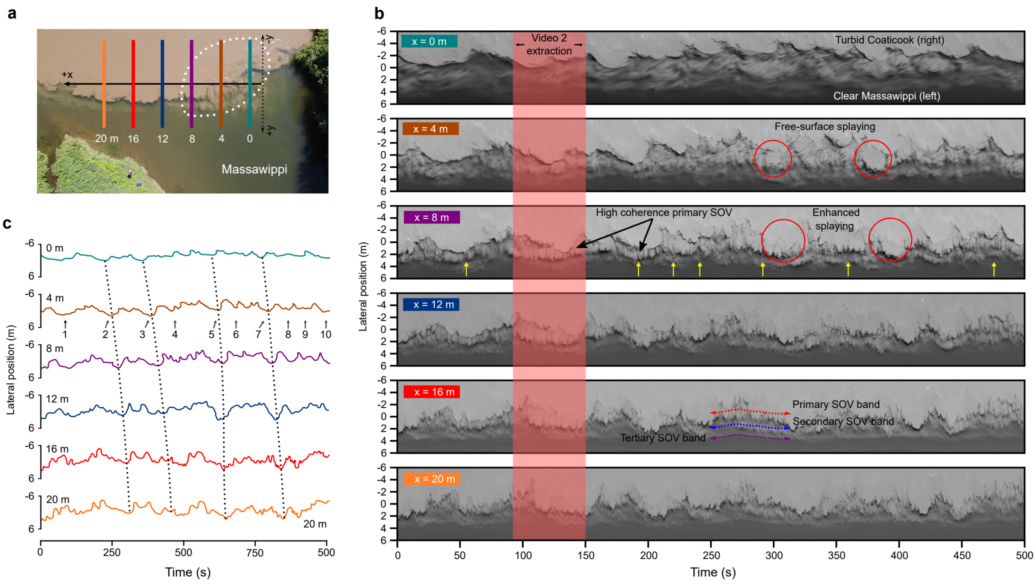

Figure 6. Space-time analysis of streamwise-orientated vortices. **a**, Locations of the 6 sampling zones used to extract pixel intensities from Video 1 to construct the space-time matrices. A white dotted line indicates the collision zone. **b**, Space-time matrices depicting the passage of surficial turbidity (lighter shades) and subsurface turbid billows (darker shades) through each sampling line over a 500 s period. At the beginning of the collision zone (i.e. $x = 0$ m), the billows streak towards the center of the mixing interface in time, confirming the billows have a clockwise sense of rotation. Red circles (at section $x = 4$ m and 8 m) indicate the onset of the primary SOV splaying under the water's surface. Yellow arrows indicate examples of darker striations consisting predominantly of clear Massawippi water. Red opaque rectangle delimits the time range of Video 2. **c**, Traces of the partition line delineating the Coaticook (turbid, light grey in Fig. 6b) and Massawippi (clear, dark grey in Fig. 6b) for each of the space-time matrices in **b**. Peaks and troughs in the traces correspond to the maximum lateral displacements of the episodic pulses (numbers 1 to 10).

The mixing interface of the $\Delta\rho_{0.0}$ case differs considerably from the drone observations in Video 1. The numerical space-time matrices in Fig. 7a, b were constructed from a similar method to that used to produce the aerial space-time matrices of Fig. 6b, however, instead of drone images, plan-view renders of 3D contours of α showing the subsurface streamwise vortices predicted in the numerical model were used as input images. The numerical space-time matrices were sampled at a frequency of 0.5 Hz. Three-dimensional shadow cast post-processing provided a realistic depth perspective in the numerical space-time matrices similar to that of the aerial drone video.

Notably, in Fig. 7a the primary, clockwise rotating SOV is not observed in the numerical space-time matrices. Rather, the mixing interface is inverted, and a strong lateral flow component of the Coaticook incurs overtop of the Massawippi (Fig. 7a, 7c, 7e). A counterclockwise rotating SOV is observed in the cross-sections of 7e. Time-series of the lateral velocity component (v) sampled near the bed and near the surface (Fig. 7g) demonstrate near-surface flow, moving predominantly towards the left bank (positive) is negatively correlated to near-bed flow moving towards the Coaticook, resulting in the counterclockwise SOV rotation. Despite the discrepancies between the $\Delta\rho = 0.0$ kg/m^3 and the drone video, the frequency (≈ 0.015 Hz), positions, and scales of the episodic pulses (Fig. 7a) are similar to observations, suggesting the pulses, unlike SOVs, are not as strongly affected by buoyancy effects.

The $\Delta\rho_{0.5}$ simulation predicts coherent flow structures within the mixing interface much better. Comparative animations of iso-contours of α (a proxy for the degree of mixing, see Methods) of the $\Delta\rho_{0.0}$ and $\Delta\rho_{0.5}$ simulations to drone imagery provide perhaps the most compelling support for the importance of density in forming the SOVs (see Video 3). Examples of the renders used to produce Video 3 are presented in Fig. 7c and d. Also, animated cross-sections at $x = 0$ m clearly show the different mixing interface dynamics of the $\Delta\rho_{0.0}$ and $\Delta\rho_{0.5}$ simulations (Video 4). The primary SOV of the $\Delta\rho_{0.5}$ simulation persists in time (Fig. 7b), and has a similar scale, position, sense of rotation, and demonstrates accurate splaying behavior as it encounters the free surface (Fig. 7b). Approximately seven episodic pulses pass during the 400 s period in Fig. 7b, for an estimated frequency of ≈ 0.018 Hz, similar to that estimated from drone observations (0.02 Hz). Also, evidence of higher-order SOVs appear in the 0.5 kg/m^3 simulations (Fig. 7b). The dynamic coupling between the primary SOV and the pulses was also predicted. Between $t = 360$ and 400 s in Supplementary Video 4 (Fig. 7f), the diameter and coherence of the primary SOV increase in a similar fashion to the primary SOV discussed in Fig. 6. Time-series of v in Fig. 7h demonstrate near-bed flow moves predominantly towards the left (positive) and is negatively correlated to near-surface flow moving towards the right, resulting in the correct clockwise rotation of the primary SOV.

5 Discussion

5.1 Densimetric Froude number

Buoyancy effects are generally considered important to confluence hydrodynamics when they significantly outweigh inertial effects (Horna-Munoz et al., 2020; Rhoads, 2020). The metric commonly used to assess the importance of $\Delta\rho$ on confluence hydrodynamics is the densimetric Froude number $\mathbf{F}_D$:

$$\mathbf{F}_D = \frac{U_0}{\sqrt{g' D}} \tag{10}$$

$$g' = \frac{(\rho_1 - \rho_2)}{\rho_1} g \tag{11}$$

where g' is reduced gravity (Eq. 11 with g the constant of gravitational acceleration, and ρ_1 and ρ_2 respectively the densities of the denser and lighter tributaries), D is a characteristic depth and U_0 is a characteristic velocity (Rhoads, 2020). In general, values of $\mathbf{F}_D << 1$ indicate $\Delta\rho$ is sufficient to cause the lighter river to flow laterally over the denser river, resulting in a vertically stratified mixing interface. In contrast, $\mathbf{F}_D >> 1$ tends towards preserving a vertical mixing interface and, at some greater value of $\mathbf{F}_D$, the influence of $\Delta\rho$ on the mixing interface becomes negligible (Rhoads, 2020).

Consensus on which length-scale and velocity scale for the calculation of $\mathbf{F}_D$ is lacking and the reason why we have avoided referring to $\mathbf{F}_D$ up to this point. $\mathbf{F}_D$ varies considerably depending on where D is chosen (e.g., average cross-sectional main channel depth, average cross-sectional tributary depth, average depth in the mixing interface) and which value of U_0 is used (e.g., a discharge-weighted average of the tributaries' bulk velocities, the bulk velocity of the tributary, or the bulk velocity of the main channel). Fischer et al. (1979) suggests that where a tributary of lighter flow enters the main channel of denser flow, the cross-sectional averages of U and D of the minor tributary are a reasonable choice. Adopting this definition for the July 9^{th}, 2020 conditions (assuming the Massawippi is the

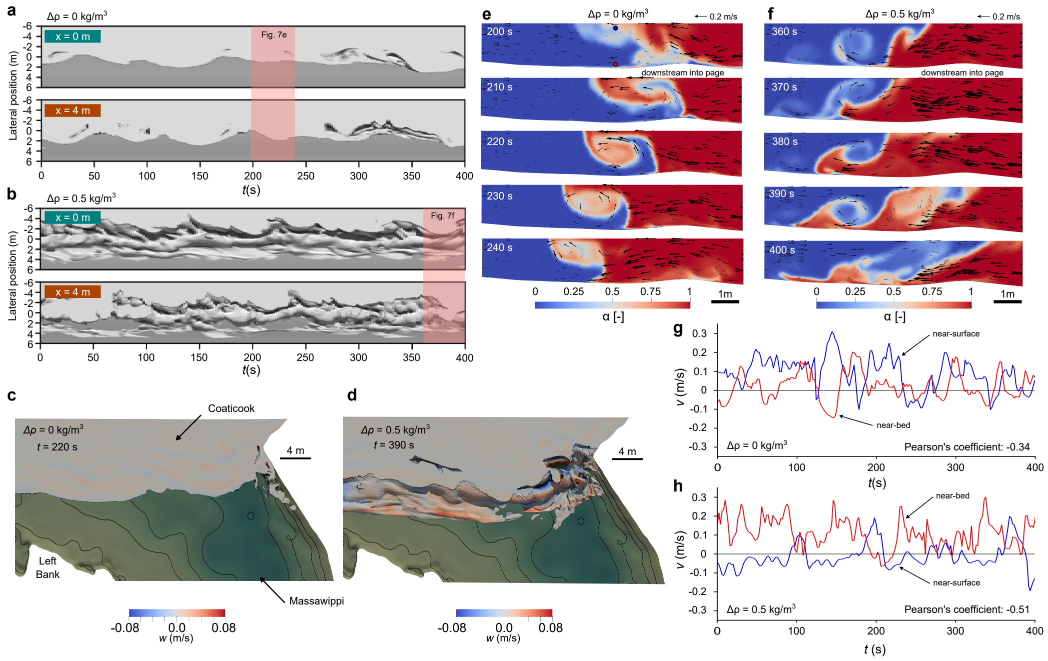

Figure 7. Comparison of eddy-resolved modeling results. **a-b**, Numerically derived space-time matrices for the $\Delta\rho_{0.0}$ and $\Delta\rho_{0.5}$ simulations. **c**, Iso-contours of $\alpha = 0.1$ (proxy indicating degree of mixing as a fractional value where 1 = Coaticook, 0 = Massawippi, see Methods) colored by w (vertical velocity) extracted from the $\Delta\rho_{0.0}$ simulation and **d** $\Delta\rho_{0.5}$ simulation showing evidence of the primary and higher order SOVs. **e - f**, Lateral cross-sections colored by α taken at $x = 0$ m (see Fig. 6a) from the $\Delta\rho_{0.0}$ and $\Delta\rho_{0.5}$ simulations, respectively. Vectors indicate secondary velocity magnitude and direction (projection of the three-dimensional velocity field ($\mathbf{u}$) onto the cross-section). **g-h**, Time-series of v (lateral component) taken 0.15 m below the surface (blue) and 0.15 m above the bed (red) at $x = 0$ m and $y = 0$ m from the $\Delta\rho_{0.0}$ and $\Delta\rho_{0.5}$ simulations (blue and red dots in **e-f** indicate sampling locations). Pearson coefficients indicate negative correlations between the near-surface and near-bed flow.

minor tributary, which strictly speaking it is not) and a $\Delta\rho$ of 0.5 kg/m^3, $\mathbf{F}_D$ would equal 1.7, indicating weak buoyancy effects. However, if $\mathbf{F}_D$ is calculated with the cross-sectional average of U and D in the Coaticook, then $\mathbf{F}_D$ is 5.5 (negligible buoyancy effects). If the definition of Horna-Munoz et al. (2020) is used (i.e., U_0 calculated as the discharge-weighted average bulk velocity of the tributaries and D the mean depth in the center of the confluence) $\mathbf{F}_D$ is 2.5, also indicating weak density effects. However, if U_0 and D are evaluated in the velocity deficit region near $x = 0$ m in Fig. 6a on the Massawippi side (i.e., $U_0 \approx 0.08$ m/s based on modeling results and $D \approx 1.6$ m) then $\mathbf{F}_D$ equals ≈ 0.9 – a value suggesting important density effects and, in the opinions of the authors, potentially a meaningful parameterization of $\mathbf{F}_D$ for the Coaticook-Massawippi confluence under this specific flow condition (but not necessarily other conditions). Therefore, regardless of how U_0 and D are defined, for the same hydraulic and density conditions, substantially different values of $\mathbf{F}_D$ and consequently, interpretations of buoyancy effects can result.

The wide range of F_D values resulting from the scaling conventions mentioned above complicates its use as a general metric for predicting density effects on confluence hydrodynamics. However, what is certain, is that even a very small value of $\Delta\rho = 0.5$ kg/m^3 (or only 0.05% the density of water at 25.5 °C) was sufficient to invert the rotation of the primary SOV and bring it from near the surface to near the bed to correctly match the observed rotation and vertical position of the SOVs in the aerial video. These are not-so-subtle effects resulting from a small value of $\Delta\rho$, the magnitude of which commonly occurs in nature. Thus, further research on how best to parameterize $\mathbf{F}_D$ is needed before it can be applied as an unambiguous predictor of density effects on a confluence's hydrodynamics.

5.2 Causal mechanism of SOVs

The SOVs observed on July 9^{th}, 2020 are distinct from previous mentions of coherent streamwise vorticity at river confluences. Our modeling shows the SOVs do not form as back-to-back cells adjacent to the mixing interface, as would be expected from the downwelling of superelevated flow mechanism discussed by others (Mosley, 1976; Paola, 1997; Constantinescu et al., 2011; Sukhodolov & Sukhodolova, 2019). Also, since the SOVs develop upstream from the avalanche face, they cannot be attributed to flow separation over this bathymetric feature (Best, 1988; Best & Roy, 1991). Also, because the SOVs were observed at a meander-bend confluence, the potential role of planform-induced secondary circulation on the SOVs merits consideration. In the numerical models, the strong curvature of the Coaticook causes a helical flow pattern on the Coaticook side (see streamlines of the mean flow field in Fig. 8) and considerable streamwise orientated vorticity within the outer bank region upstream of the confluence's apex (see isocontours of Q-criterion in Video 5). However, both the helical flow and outer bank vorticity are considered to play little to no role in the formation of the observed SOVs. Identical helical flow patterns (see Fig. 8) and outer bank flow structure were predicted in both the $\Delta\rho_{0.0}$ and $\Delta\rho_{0.5}$ simulations (see Video 5), yet only the $\Delta\rho_{0.5}$ simulation correctly reproduced the sense of rotation of the observed SOVs. Finally, their strong coherence within the mixing interface observed in the aerial video, and well-defined lateral left-hand limit, indicate the SOVs are spatially independent of curvature-induced helical motions mentioned in previous studies (Rhoads & Kenworthy, 1995; Sukhodolov & Rhoads, 2001; Riley et al., 2015; Rhoads & Johnson, 2018; Sukhodolov & Sukhodolova, 2019).

Here we attempt to explain the causal mechanism of the observed SOVs. First, where the rivers meet at the apex, the density difference between the Coaticook and Massawippi causes a hydrostatic pressure gradient across the mixing interface. The gradient accelerates a front of dense Coaticook laterally along the bed underneath the partition line towards the Massawippi side of the confluence (similar to that expected of a 2D finite volume gravity current or *lock-exchange* (Rottman & Simpson, 1983; Cantero et al., 2007)). As the dense Coaticook falls and extends laterally, an equivalent volume of light Massawippi is pulled laterally in the opposite direction to replace the fallen volume of Coaticook (also similar to that expected in a 2D fixed-volume lock-exchange). This initiates a cross-flow over the vertical axis of the mixing interface. Without continuous flow arriving from upstream in each channel, this cross-flow would extend to the banks of the confluence. However, its lateral propagation is inhibited by the converging lateral flow components of each tributary as they converge and advect downstream. The lateral positions at which the propagation of the leading fronts of the cross-flow stop occurs where their lateral momentum is balanced by those of the tributaries they are pushing into. Where this occurs near the bed, the light Massawippi moves overtop the dense front of the Coaticook, deflecting it and causing it to curl back above itself. The near-surface movement of the lighter Massawippi explains the persistent layer of clear water between the SOV and the free surface in the drone observations of Fig. 5 (also conceptually illustrated in Fig. 9). Where the lateral momentum of the light near-surface front equals that of the opposing Coaticook, its momentum is then redirected downwards (on the surface, this location can be identified by the partition line in Fig. 5d).

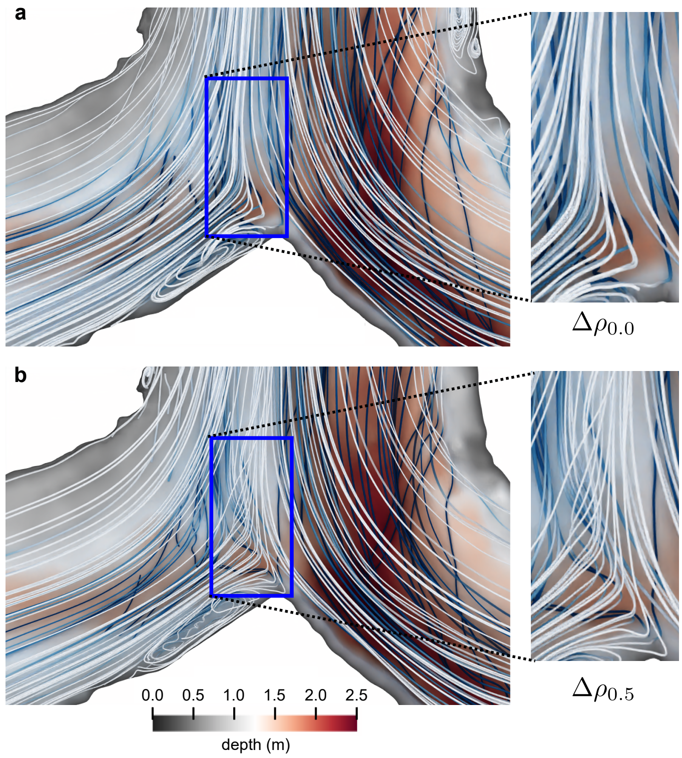

Figure 8. Streamlines of mean numerical flow fields. Streamlines of the mean flow field ($\overline{U}$) showing the fate of near-bed (darker blue) and near-surface flow (lighter shades of blue) in the a) $\Delta\rho_{0.0}$ and b) $\Delta\rho_{0.5}$ simulations. Small differences in streamlines are caused by random streamline seeding locations upstream in both tributaries. The bathymetry is colored by depth. A vertical exaggeration factor of 3 is applied to emphasize the 3D aspects of the flow. No important deviations are observed between the streamlines of the two conditions in the upstream portion of the Coaticook. The only notable difference is the streamlines indicating clockwise rotation on the left-hand side of the mixing interface downstream of the apex. In the blue rectangle of (b) ($\Delta\rho_{0.5}$) streamlines entering from the Massawippi descend from near the surface to the bed and then back towards the surface in a spiraling motion. In contrast, the streamlines of (a) remain relatively parallel to the bed as they travel through this zone.

Finally, the net effect of the redirected momentum of the dense and light front results in the formation of the stunningly coherent streamwise orientated vortices observed in Videos 1 and 2. Because this process is initiated by $\Delta\rho$ - a mean property of the confluence's flow field - the SOVs, despite their obvious turbulent character in the drone videos, are nevertheless thought to inherently be coherent structures of the mean flow field.

Preliminary simulations considering $\Delta\rho > 0.5$ kg/m^3 demonstrated that additional $\Delta\rho$ causes the front to extend farther towards the left bank. In these preliminary simulations, the shear developed at the tilted interface of the ensuing stratified layers generates one or more larger width SOVs. However, a unique value of $\Delta\rho$ exists ($\approx \Delta\rho = 0.5$ kg/m^3 in this study), at which inertial and buoyant forces balance in such a way as to cause a highly coherent, near-circular primary SOV to develop. This value of $\Delta\rho$ and the diameter of the SOV it produces are expected to be functions most of the velocity and depth of the converging tributaries in the *immediate* region of the mixing interface.

In essence, the observed SOVs are a class of gravity current whose lateral propagation is continuously inhibited by the opposing momentum of the incoming tributaries as the current is advected downstream. The gravity current, therefore, is 'confined' within the SOV. Consequently, in contrast to channel-scale density effects (Horna-Munoz et al., 2020), the analogy of the mixing interface of a confluence of two rivers of unequal density to a fixed-volume, 2D lock-exchange flow fails to fully capture the important 3D hydrodynamic processes responsible for the development of the observed/modeled cells. Further work towards a scale-independent understanding of this type of confined 3D gravity current with attempts to account for the influence of other sources of streamwise vorticity (e.g. curvature induced superelevation and avalanche face flow separation) is required. Tentatively, the term *density* SOV is proposed to conveniently refer to the SOVs in the aerial video as it emphasizes the important role of density gradients in their formation.

6 Conclusion

This study provides tenable empirical evidence of streamwise orientated vortices dynamically coupled to episodic pulses in the mixing interface of a natural mesoscale confluence. Numerical modeling suggests the observed SOVs formed due to a small difference in density between the Coaticook and Massawippi on July 9th 2020 (with the Coaticook being $\approx$ 0.5 kg/m^3 denser than the Massawippi). The aerial observations also provide compelling

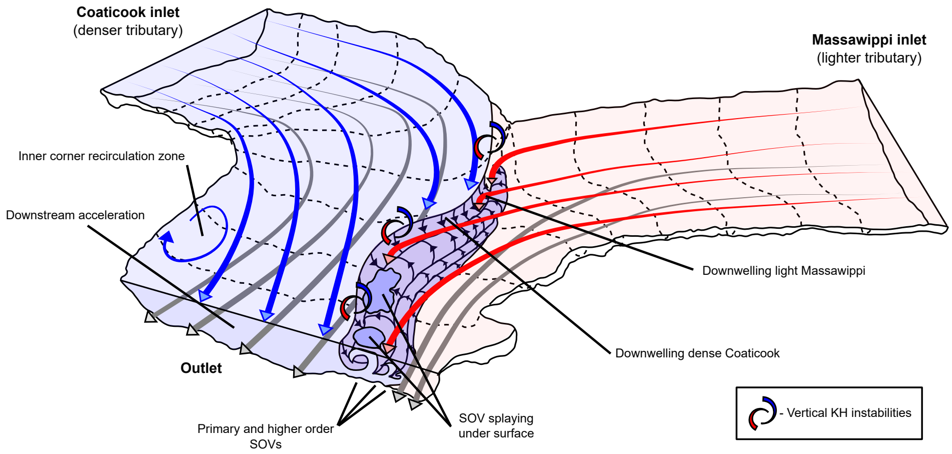

Figure 9. Conceptual model. Conceptual depiction of coherent flow structure interactions within the mixing interface of the Coaticook-Massawippi meander-bend confluence for the flow conditions of July 9^{th}, 2020 (Coaticook denser by ≈ 0.5 kg/m^3).

evidence the density SOVs are spatially distinct from planform-induced helical flow present within the confluence and that the SOVs were not effective in driving lateral mixing within the postconfluent reach. The *density* SOVs are a confined gravity current which results as the lateral momentum components of the near-bed dense front and near-surface light front being confined by the opposing momentum of the converging tributaries. Our studies' findings were possible by combining aerial observations of turbidity gradients with eddy-resolved numerical modeling and thus demonstrate a promising approach for confluence hydrodynamic research.

Our study also raises several research questions for future field, numerical and experimental work. First, how can the proposed density-driven causal mechanism be reconciled with the downwelling of superelevated flow mechanism and planform curvature-induced secondary currents largely attributed to the formation of SOVs and helical secondary flow cells in previous studies (Mosley, 1976; Rhoads & Kenworthy, 1995; Paola, 1997; Sukhodolov & Rhoads, 2001; Riley et al., 2015; Rhoads & Johnson, 2018; Sukhodolov & Sukhodolova, 2019)? Second, does an appropriate scaling convention for the densimetric Froude number exist permitting an unambiguous metric for assessing density effects on a confluence's hydrodynamics? Third, can an analytically or empirically theory be derived to explain the formation of the observed density SOVs? If so, can these explanations also incorporate effects of superelevation, planform-induced secondary flow, and avalanche face separation (bathymetric feedback effects)? Given the important impact of $\Delta\rho$ on the character of the mixing interface and considering that such small density differences are likely the rule rather than the exception at natural confluences, answers to these questions will be necessary in the pursuit of a unified conceptual model of confluence hydrodynamics, mixing and sediment transport processes.

7 Open Research

The data that support the findings of this study are openly available in the collection "Coaticook-Massawippi confluence" on "figshare" at https://doi.org/10.6084/m9.figshare.c.5343626.v1

Acknowledgments

The authors would like to thank the Fonds de Recherche du Québec - Nature et technologies (FRQNT) for supporting the BX3 postdoctoral research scholarship which funded the majority of this research. The Natural Science and Engineering Research Council of Canada Discovery grant of Pascale Biron also supported this research. Simulations were made possible by the computational clusters supported by the team at Compute Canada. The contribution of Compute Canada, its principal funding agency The Canada Foundation for Innovation (CFI) and Compute Canada's supporting academic and provincial partners cannot be overstated.

8 Figure Captions

8.1 Figure 1

Massawippi-Coaticook meander-bend confluence. **a**, High-elevation planform geometry of the confluence located in the province of Quebec, Canada (45°18'50"N 71°53'55"W). At high discharge, the Coaticook, which flows through an agricultural watershed is generally turbid. The Massawippi, flowing through a forested watershed is often clear. **b**, Planform characteristics and hydrodynamic zones on a high elevation view of the confluence taken at 15:41:00 UTC on July 9^{th}, 2020. **c**, Bathymetry of the confluence colored by depth below the free surface (146.07 m above sea level) during the numerical model validation field campaign of October 22^{nd}, 2020. Water surface elevation was 0.07 m higher on July 9^{th} (146.14

m above sea level) than on October 22^{nd}, 2020. Contoured region delimits extents of the numerical modeling domain. Black contoured circles indicate locations of the four ground reference points for large-scale particle image velocimetry measurements of October 22^{nd}, 2020. Locations of propeller current meter profiles are indicated with blue dots (a-g).

8.2 Figure 2

High elevation view of confluence planform. Aerial view of the Coaticook-Massawippi confluence on November 15^{th}, 2020 under clear-water conditions taken approximately 200 m above the confluence. Image included to emphasis the meander-like bend the Coaticook makes as it joins the post-confluent channel. Dune formations visible upstream of the apex in the Coaticook.

8.3 Figure 3

Mean surface velocity comparison of LSPIV and WMLES data. **a**, Surface distribution of $\overline{U}_{uv}$ with streamlines indicating mean flow direction obtained with large-scale particle image velocimetry on taken on October 22^{nd}, 2020 (magnitude of mean streamwise and lateral velocity vector components). Contours delimit zone of valid vectors. **b**, Distribution of $\overline{U}_{uv}$ on the surface predicted by wall-modelled large-eddy simulation (WMLES).

8.4 Figure 4

Comparison of numerical and measured velocity profiles over depth. **a-f**, Comparison of predicted (WMLES) vertical profiles of $\overline{U}$ to measured profiles obtained with a current meter at the 7 sampling locations (see Fig. 1c) on October 22^{nd}, 2020. z is the height above the bed and h is the depth at the sampling location.

8.5 Figure 5

Life-cycle dynamics of the primary SOV. a-i Still images extracted at 7.5 s intervals from Video 2. t starts at the beginning of Video 2. The loosely coherent subsurface turbid waters of the Coaticook (**a**) are observed to rapidly cohere (**b**, **c**, **d**) as the episodic pulse advances to its farthest location (**e**) at ≈ 30 s into the cycle. As the pulse recedes, the coherence of the primary SOV diminishes (**g-i**). Black arrows (**a**) indicate mean direction of incoming surface flows. Black bars placed at fixed locations in each subplot to assist visualisation of the lateral migration of the mixing interface with time. Red bars indicate approximate lateral limit of the advancing partition line of the episodic pulse (sharp gradient on surface between turbid and clear water, identified by a white dot-dashed line in **d**). Blue bars indicate approximate left limit of the primary SOV. During the passage of this typical episodic pulse, the left-most limit of the primary SOV maintains approximately the same lateral position, despite the partition line translating left by upwards of 1.9 m.

8.6 Figure 6

Space-time analysis of streamwise-orientated vortices. a, Locations of the 6 sampling zones used to extract pixel intensities from Video 1 to construct the space-time matrices. White dotted line indicates the collision zone. **b**, Space-time matrices depicting the passage of surficial turbidity (lighter shades) and subsurface turbid billows (darker shades) through each sampling line over a 500 s period. At the beginning of the collision zone (i.e. $x = 0$ m), the billows streak towards the centre of the mixing interface in time, confirming the billows have a clockwise sense of rotation. Red circles (at section $x = 4$ m and 8 m) indicate the onset of the primary SOV splaying under the water's surface. Yellow arrows indicate examples of darker striations consisting predominantly of clear Massawippi water. Red opaque rectangle delimits the time range of Video 2. **c**, Traces of the partition line delineating the Coaticook (turbid, light grey in Fig. 6b) and Massawippi (clear, dark grey in Fig. 6b) for each of the space-time matrices in **b**. Peaks and troughs in the traces correspond to the maximum lateral displacements of the episodic pulses (numbers 1 to 10).

8.7 Figure 7

Comparison of eddy-resolved modeling results. **a-b**, Numerically derived space-time matrices for the $\Delta\rho_{0.0}$ and $\Delta\rho_{0.5}$ simulations. **c**, Iso-contours of $\alpha = 0.1$ (proxy indicating degree of mixing as a fractional value where 1 = Coaticook, 0 = Massawippi, see Methods) colored by w (vertical velocity) extracted from the $\Delta\rho_{0.0}$ simulation and **d** $\Delta\rho_{0.5}$ simulation showing evidence of the primary and higher order SOVs. **e - f**, Lateral cross-sections colored by α taken at $x = 0$ m (see Fig. 6a) from the $\Delta\rho_{0.0}$ and $\Delta\rho_{0.5}$ simulations, respectively. Vectors indicate secondary velocity magnitude and direction (projection of the three-dimensional velocity field ($\mathbf{u}$) onto the cross-section). **g-h**, Time-series of v (lateral component) taken 0.15 m below the surface (blue) and 0.15 m above the bed (red) at $x = 0$ m and $y = 0$ m from the $\Delta\rho_{0.0}$ and $\Delta\rho_{0.5}$ simulations (blue and red dots in **e-f** indicate sampling locations). Pearson coefficients indicate negative correlations between the near-surface and near-bed flow.

8.8 Figure 8

Streamlines of mean numerical flow fields. Streamlines of the mean flow field ($\overline{U}$) showing the fate of near-bed (darker blue) and near-surface flow (lighter shades of blue) in the a) $\Delta\rho_{0.0}$ and b) $\Delta\rho_{0.5}$ simulations. Small differences in streamlines are caused by random streamline seeding locations upstream in both tributaries. The bathymetry is colored by depth. A vertical exaggeration factor of 3 is applied to emphasis 3D aspects of the flow. No important deviations are observed between the streamlines of the two conditions in the upstream portion of the Coaticook. The only notable difference is the streamlines indicating clockwise rotation on the left hand-side of the mixing interface downstream of the apex. In the blue rectangle of (b) ($\Delta\rho_{0.5}$) streamlines entering from the Massawippi descend from near the surface to the bed and then back towards the surface in a spiralling motion. In contrast, the streamlines of (a) remain relatively parallel to the bed as they travel through this zone.

8.9 Figure 9

Conceptual model. Conceptual depiction of coherent flow structure interactions within the mixing interface of the Coaticook-Massawippi meander-bend confluence for the flow conditions of July 9^{th}, 2020 (Coaticook denser by ≈ 0.5 kg/m^3).

9 Supplementary Information

9.1 Aerial flow field overview

It is valuable to describe the important features of the confluence's flow field based on qualitative observation of drone video. First, a sharp turbidity contrast develops on the surface where the two rivers meet (Video 6). This partition line delineates the Coaticook from the Massawippi side of the confluence. At the discharge ratio (Q_r) of 4.66 on July 9^{th}, 2020, the high discharge, turbid Coaticook confines the relatively clear Massawippi to a narrow region near the left downstream corner of the confluence, the width of which varies between 8 and 12 m with the passage of the episodic pulses. Flow in the confined region is shallow, with depths ranging between 0.4 and 1 m. Downstream of the confluence apex, the mixing interface continues approximately along the path of curvature established by the outer bank of the preconfluent Coaticook for $\approx$ 10 m ($0.30B$). Farther downstream, the curvature is thwarted by the confined Massawippi, causing the mixing interface to deflect and continue along a nearly straight trajectory for $\approx$ 45 m ($1.33B$) (between 40 and 60 ° Fig. 1c) before again curving to align with the downstream postconfluent channel (after 60 ° Fig. 1c). The mixing interface first 'bends' over the deepest portion of the Massawippi where depths vary between 1.3 and 1.7 m (Fig. 1c) caused by thalweg scour during more common flow conditions such as those of October 22nd, where $Q_r \approx 1$ (since drainage areas of both incoming rivers are similar). The coherence and dynamics of the streamwise vortices are most apparent in the mixing interface between 30 and 50 ° (Fig. 1b). The position of the mixing interface along this stretch varies between 7 and 10 m (0.21 to $0.30B$) to the left (west) of the scour hole on the Coaticook side.

On the Coaticook side in Video 6, a distinct line of glare reflects off of surface disturbances near the upstream portion of the inside corner of the Coaticook (Fig. 1b). The shape and position of the disturbances are consistent with that of an inner bank recirculatory cell common to meander bends of strong curvature (Ferguson et al., 2003). Converging trajectories of surface glare and foam advecting into the confluence in the middle of the Coaticook in Video 6 suggests the presence of a central secondary flow cell typical of meander bends (Booij, 2003; Blanckaert & de Vriend, 2004). The converging trajectories continue to within $\approx$ 3 m of the outside bank of the Coaticook where surface foam from the central flow region is observed to collect into a line. Surface flow patterns suggest a distinct outer-bank cell is present between the red dotted line Fig. 1c and the outer bank of the Coaticook (Booij, 2003; Blanckaert & de Vriend, 2004).

Sufficient surface particles are visible on the Massawippi side of the confluence in Video 1 to qualitatively discuss surface flow patterns. Notably, near the apex of the confluence, a region of backflow extends upstream along a short section of the outer bank of the Coaticook. This region combined with a volume of nearly stalled flow adjacent to the apex on the Massawippi side forms a small stagnation zone that extends $\approx$ 5 m ($0.15B$) laterally from the apex into the Massawippi (Fig. 1b). Farther downstream, slow movements of floating particles converging towards the mixing interface can be observed in Video 1 for $\approx$ 8-12 m (0.24 to $0.36B$) from the terminal point of the stagnation zone on the Massawippi side. The lateral momentum of the colliding tributaries is strongest over this 'collision' zone (Fig. 1c). Over the narrow and shallow confined region of clear flow near the left bank, surface particles follow the flow curvature near the left downstream corner as it aligns with the postconfluent flow. Flow within the confined region rapidly accelerates as it becomes increasingly confined passing over the shallow bathymetry (Video 1). Mixing as observed by the lateral transfer of turbidity is seen to be limited until past 70 ° in Fig. 1b.

10 Video captions

10.1 Video 1

Long duration aerial drone video taken of the Coaticook-Massawippi confluence's mixing interface on July 9^{th}, 2020 at 14:41:00 (UTC). The formation of the turbid streamwise orientated vortices (SOVs) is visible through the relatively clear waters of the Massawippi. The SOVs are observed to dynamically interact with the passing of the lateral episodic pulses.

10.2 Video 2

A minute-long extract taken from Video 1 playing at 1x on the left and at 8x on the right (which then repeats 8 times). The rotation of the primary streamwise vortex, made visible by the contrast in turbidity between the two channels, rotates clockwise around a streamwise axis pointing downstream on the clear Massawippi side of the partition line. The coherence of the vortex increases as the episodic pulse from the Coaticook sweeps the SOV towards the left bank of the confluence. A smaller diameter secondary SOV is also observed to form, also with a clockwise sense of rotation to the left of the primary SOV. Near the apex, the dense turbid billows of the Coaticook move laterally left within the lower portion of the water column.

10.3 Video 3

Comparison of (a) Video 1 to iso-contours of α set at 0.1 and colored by the vertical velocity component for both the (b) $\Delta\rho_{0.0}$ simulation and the (c) $\Delta\rho_{0.5}$ simulation. Playback speed of 8x. Though coherent vortices (generally with a counter-clockwise sense of rotation) are predicted in the $\Delta\rho_{0.0}$ simulation (see Fig. 4e), they are largely obscured by a near-surface layer containing a significant proportion of water from the Coaticook. Nevertheless, episodic pulses are still present along the mixing interface in the $\Delta\rho_{0.0}$ results. In contrast, the $\Delta\rho_{0.5}$ simulation accurately predicts the clockwise sense of rotation of the primary SOV, the episodic pulses and shows evidence of secondary and tertiary vortices to its left. Overall the $\Delta\rho = 0.5$ kg/m^3 predictions match the aerial observations well.

10.4 Video 4 caption

Cross-sections of α taken at $x = 0$ m (see Fig. 3a) showing the subsurface turbulent flow structure for the (a) $\Delta\rho_{0.0}$ simulation and the (b) $\Delta\rho_{0.5}$. Vectors indicate secondary flow directions resulting from projecting the three-component velocity field onto the cross-section. Red indicates water from the Coaticook, while blue indicates water from the Massawippi. The cross-section is looking downstream. Playback speed of video equal to 8x. Streamwise vorticity in the $\Delta\rho_{0.0}$ generally occurs counterclockwise around the streamwise axis facing downstream. In contrast, evidence of clockwise rotating primary and higher-order streamwise vortices can be observed in the $\Delta\rho_{0.5}$ results.

10.5 Video 5 caption

Comparison of iso-contours of Q-criterion within the confluence for the $\Delta\rho_{0.0}$ (top) and $\Delta\rho_{0.0}$ (bottom) colored by vertical velocity component. Playback speed at 8x. Passing iso-contours of Q-criterion identify coherent turbulent structures within the flow. The turbulent flow structure in the preconfluent branch of the Coaticook is identical in both simulations. Within the mixing interface, however, the $\Delta\rho_{0.0}$ simulation predicts streamwise coherent structures to have a predominantly counterclockwise sense of rotation, whereas in the $\Delta\rho_{0.5}$ the isocontours rotate in the clockwise direction consistent with drone observations.

10.6 Video 6 caption

High elevation aerial drone video of the Massawippi-Coaticook confluence taken at 15:41 UTC on July 9^{th}, 2020 (approximately 100 m above confluence). Coherent streamwise vortices are observed to rotate clockwise within the mixing interface. The advection of episodic pulses and smaller-scale vertically orientated Kelvin-Helmholtz vortices are also noted along the mixing interface. Glare reflecting off surface disturbances near the inside corner of the Coaticook (turbid channel) indicates the presence of an inside-side bank separation cell common to meander bends. A line of surface foam collects near the outside bank of the Coaticook, suggesting the presence of an outer bank cell. Lateral mixing of the turbid water of the Coaticook is limited along the confluence until the flow reaches the farthest downstream section where an abrupt turn aligns the flow with the postconfluent channel.

10.7 Numerical modeling details

Table 2. Discretization schemes

Dictionary name	Subdictionary	Entry
ddtSchemes		
	default	backward
gradSchemes		
	default	Gauss linear
divSchemes		
	div(rhophi, U)	Gauss vanLeer
	div(phi, alpha)	Gauss limitedLinear01 1
	div(phi,nuTilda)	Gauss upwind
	div((muEff*dev(T(grad(U)))))	Gauss linear
	div((rho*nuEff)*dev2(T(grad(U)))))	Gauss linear
laplacianSchemes		
	default	Gauss linear corrected
interpolationSchemes		
	default	linear

References

Best, J. L. (1988). Sediment transport and bed morphology at river channel confluences. *Sedimentology*, *35*, 481–498.

Best, J. L., & Roy, A. G. (1991). Mixing-layer distortion at the confluence of channels of different depth. *Nature*, *350*, 411–413.

Biron, P. M., Buffin-Bélanger, T., & Martel, N. (2019). Three-dimensional turbulent structures at a medium-sized confluence with and without an ice cover. *Earth Surface Processes and Landforms*, *3056*, 3042–3056.

Biron, P. M., & Lane, S. N. (2008). Modelling hydraulics and sediment transport at river confluences. In *River confluences, tributaries and the fluvial network* (pp. 17–43).

Table 3. OpenFOAM boundary conditions

field	inlets	outlet	walls	surface	units
nut	zeroGradient	zeroGradient	nutURoughWallFunction	symmetry	[m^2/s]
prgh	zeroGradient	fixedValue 0	zeroGradient	symmetry	[kgm/s^2]
u	turbulentDFSEMInlet	inletOutlet 0	fixedValue 0	symmetry	[m/s]
alpha	fixedValue (1 Coaticook, 0 Massawippi)	zeroGradient	zeroGradient	symmetry	[-]

Blanckaert, K., & de Vriend, H. J. (2004). Secondary flow in sharp open-channel bends. *Journal of Fluid Mechanics*, *498*, 353–380.

Booij, R. (2003). Measurements and large eddy simulations of the flows in some curved flumes. *Journal of Turbulence*, *4*, 37–41.

Cantero, M. I., Lee, J. R., Balachandar, S., & Garcia, M. H. (2007). On the front velocity of gravity currents. *Journal of Fluid Mechanics*, *586*, 1–39.

Celik, I. B., Cehreli, Z. N., & Yavuz, I. (2005, 09). Index of Resolution Quality for Large Eddy Simulations. *Journal of Fluids Engineering*, *127*(5), 949-958. doi: 10.1115/1.1990201

Cheng, Z., & Constantinescu, G. (2020). Stratification effects on hydrodynamics and mixing at a river confluence with discordant bed. *Environmental Fluid Mechanics*, *20*, 843–872.

Constantinescu, G. (2014). LE of shallow mixing interfaces: A review. *Environmental Fluid Mechanics*, *14*, 971–996.

Constantinescu, G., Miyawaki, S., Rhoads, B., & Sukhodolov, A. (2012). Numerical analysis of the effect of momentum ratio on the dynamics and sediment-entrainment capacity of coherent flow structures at a stream confluence. *Journal of Geophysical Research: Earth Surface*, *117*, 1–21.

Constantinescu, G., Miyawaki, S., Rhoads, B., & Sukhodolov, A. (2016). Influence of planform geometry and momentum ratio on thermal mixing at a stream confluence with a concordant bed. *Environmental Fluid Mechanics*, *16*, 845–873.

Constantinescu, G., Miyawaki, S., Rhoads, B., Sukhodolov, A., & Kirkil, G. (2011). Structure of turbulent flow at a river confluence with momentum and velocity ratios close to 1: Insight provided by an eddy-resolving numerical simulation. *Water Resources Research*, *47*, 1–16.

da Vinci L. (2009). *The Notebooks of Leonardo da Vinci* (Vol. 2; E. MacCurdy, Trans.). The Folio Society.

De Serres, B., Roy, A. G., Biron, P. M., & Best, J. L. (1999). Three-dimensional structure of flow at a confluence of river channels with discordant beds. *Geomorphology*, *26*, 313–335.

Duguay, J., Biron, P., & Buffin-Bélanger, T. (2022). Large-scale turbulent mixing at a mesoscale confluence assessed through drone imagery and eddy-resolved modelling. *Earth Surface Processes and Landforms*, *47*(1), 345-363.

Ferguson, R. I., Parsons, D. R., Lane, S. N., & Hardy, R. J. (2003). Flow in meander bends with recirculation at the inner bank. *Water Resources Research*, *39*, 0–13.

Fischer, H. B., List, J. E., Koh, R., Imberger, J., & B. H. Brooks, N. (1979). *Mixing in inland and coastal waters.* San Diego: Academic Press.

Grbčič, L., Kranjčević, L., Lučin, I., & Čarija, Z. (2019). Experimental and numerical investigation of mixing phenomena in double-Tee junctions. *Water (Switzerland)*, *11*(6).

Gruber, M. F., Johnson, C. J., Tang, C. Y., Jensen, M. H., Yde, L., & Hélix-Nielsen, C. (2011). Computational fluid dynamics simulations of flow and concentration polarization in forward osmosis membrane systems. *Journal of Membrane Science*, *379*(1-2), 488–495.

Guillén Ludeña, S., Cheng, Z., Constantinescu, G., & Franca, M. J. (2017). Hydrodynamics of mountain-river confluences and its relationship to sediment transport. *Journal of Geophysical Research: Earth Surface*, *122*, 901–924.

Horna-Munoz, D., Constantinescu, G., Rhoads, B., Lewis, Q., & Sukhodolov, A. (2020). Density effects at a concordant bed natural river confluence. *Water Resources Research*, *56*.

Jones, F. E., & Harris, G. L. (1992). ITS-90 Density of Water Formulation for Volumetric Standards Calibration. *Journal of research of the National Institute of Standards and Technology*, *97(3)*, 335–340.

Kara, S., Kara, M. C., Stoesser, T., & Sturm, T. W. (2015). Free-surface versus rigid-lid LES computations for bridge-abutment flow. *Journal of Hydraulic Engineering*, *141*, 1–9.

Keylock, C. J., Constantinescu, G., & Hardy, R. J. (2012). The application of computational fluid dynamics to natural river channels: Eddy resolving versus mean flow approaches. *Geomorpholgy*, *179*, 1–20.

Khosronejad, A., Arabi, M. G., Angelidis, D., Bagherizadeh, E., Flora, K., & Farhadzadeh, A. (2020). A comparative study of rigid-lid and level-set methods for LES of open-channel flows: morphodynamics. *Environmental Fluid Mechanics*, *20*(1), 145–164.

Khosronejad, A., Flora, K., & Kang, S. (2020). Effect of inlet turbulent boundary conditions on scour predictions of coupled LES and morphodynamics in a field-scale river : Bankfull flow conditions. *Journal of Hydraulic Engineering*, *146*, 1–24.

Khosronejad, A., Ghazian Arabi, M., Angelidis, D., Bagherizadeh, E., Flora, K., &

Farhadzadeh, A. (2019). Comparative Hydrodynamic Study of Rigid-Lid and Level-Set Methods for LES of Open-Channel Flow. *Journal of Hydraulic Engineering*, *145*(1), 04018077. doi: 10.1061/(asce)hy.1943-7900.0001546

Lai, A. C., Zhao, B., Law, A. W. K., & Adams, E. E. (2015). A numerical and analytical study of the effect of aspect ratio on the behavior of a round thermal. *Environmental Fluid Mechanics*, *15*(1), 85–108.

Lane, S. N., Parsons, D. R., Best, J. L., Orfeo, O., Kostaschuk, R. A., & Hardy, R. J. (2008). Causes of rapid mixing at a junction of two large rivers: Río Paraná and Río Paraguay, Argentina. *Journal of Geophysical Research: Earth Surface*, *113*, 1–16.

Le, T. B., Khosronejad, A., Sotiropoulos, F., Bartelt, N., Woldeamlak, S., & Dewall, P. (2019). Large-eddy simulation of the Mississippi River under base-flow condition: hydrodynamics of a natural diffluence-confluence region. *Journal of Hydraulic Research*, *57*, 836–851.

Lewis, Q. W., & Rhoads, B. L. (2015). Resolving two-dimensional flow structure in rivers using large-scale particle image velocimetry: An example from a stream confluence. *Water Resources Research*, *51*, 7977–7994. doi: 10.1002/2015WR017200.A

Lewis, Q. W., & Rhoads, B. L. (2018). LSPIV measurements of two-dimensional flow structure in streams using small unmanned aerial systems: 2. Hydrodynamic mapping at river confluences. *Water Resources Research*, *54*, 7981–7999.

Mosley, P. (1976). An experimental study of channel confluences. *The Journal of Geology*, *84*, 535–562.

Moukalled, F., Mangani, L., & Darwish, M. (2016). *The finite volume method in computational fluid dynamics* (Vol. 113). Springer International Publishing.

Paola, C. (1997). When streams collide. *Nature*, *387*, 232–233.

Poletto, R., Craft, T., & Revell, A. (2013). A new divergence free synthetic eddy method for the reproduction of inlet flow conditions for les. *Flow, Turbulence and Combustion*, *91*, 519–539.

Pope, S. B. (2011). *Turbulent flows.* Cambridge: Cambridge Univ. Press.

Rhoads, B. L. (2020). The Dynamics of River Confluences. In *River dynamics: geomorphology to support management* (pp. 269–293). Cambridge University Press.

Rhoads, B. L., & Johnson, K. K. (2018). Three-dimensional flow structure, morphodynamics, suspended sediment, and thermal mixing at an asymmetrical river confluence of a straight tributary and curving main channel. *Geomorphology*, *323*, 51–69.

Rhoads, B. L., & Kenworthy, S. T. (1995). Flow structure at an asymmetrical stream confluence. *Geomorphology*, *11*(4), 273-293.

Rhoads, B. L., & Kenworthy, S. T. (1999). On secondary circulation, helical motion and rozovskii-based analysis of time-averaged two-dimensional velocity fields at confluences. *Earth Surface Processes and Landforms*, *24*(4), 369-375.

Rhoads, B. L., & Sukhodolov, A. N. (2001). Field investigation of three-dimensional flow structure at stream confluences: 1. Thermal mixing and time-averaged velocities. *Water Resources Research*, *37*, 2393–2410.

Riley, J. D., Rhoads, B. L., Parsons, D. R., & Johnson, K. K. (2015). Influence of junction angle on three-dimensional flow structure and bed morphology at confluent meander bends during different hydrological conditions. *Earth Surface Processes and Landforms*, *40*, 252–271.

Rodi, W., Constantinescu, G., & Stoesser, T. (2014). *Large-eddy simulation in hydraulics.* CRC Press.

Rogers, M. M., & Moser, R. D. (1992). The three-dimensional evolution of a plane mixing layer: the kelvin–helmholtz rollup. *Journal of Fluid Mechanics*, *243*, 183–226.

Rottman, J. W., & Simpson, J. E. (1983). Gravity currents produced by instantaneous releases of a heavy fluid in a rectangular channel. *Journal of Fluid Mechanics*, *135*, 95–110.

Sabrina, S., Lewis, Q., & Rhoads, B. (2021). Large-scale particle image velocimetry reveals pulsing of incoming flow at a stream confluence. *Water Resources Research*, *57*(9), e2021WR029662.

Saguat, P. (2001). *Large Eddy Simulation for Incompressible Flows: An Introduction.* Berlin: Springer.

Schindfessel, L., Creëlle, S., & De Mulder, T. (2015). Flow patterns in an open channel confluence with increasingly dominant tributary inflow. *Water (Switzerland)*, *7*, 4724–4751.

Smagorinsky, J. (1963). General circulation experiments with the primitive equations. *Monthly Weather Review*, *91*, 99-164.

Sukhodolov, A. N., & Rhoads, B. L. (2001). Field investigation of three-dimensional flow structure at stream confluences: 2. Turbulence. *Water Resources Research*, *37*, 2411–2424.

Sukhodolov, A. N., & Sukhodolova, T. A. (2019). Dynamics of flow at concordant gravel bed river confluences: Effects of junction angle and momentum flux ratio. *Journal of Geophysical Research: Earth Surface*, *124*, 588–615.

Van Balen, W., Uijttewaal, W. S., & Blanckaert, K. (2009). Large-eddy simulation of a mildly curved open-channel flow. *Journal of Fluid Mechanics*, *630*, 413–442.

van Rooijen, E., Mosselman, E., Sloff, K., & Uijttewaal, W. (2020). The effect of small density differences at river confluences. *Water (Switzerland)*, *12*, 1–18.

Weller, H. G., Tabor, G., Jasak, H., & Fureby, C. (1998). A tensorial approach to computational continuum mechanics using object-oriented techniques. *Computers in Physics*, *12*, 620-631.

Wolman, G. M. (1954). A method of sampling coarse river-bed material. *Eos Transactions American Geophysical Union*, *35*, 951-956.

Yuan, S., Tang, H., Li, K., Xu, L., Xiao, Y., Gualtieri, C., ... Melville, B. (2021). Hydrodynamics, sediment transport and morphological features at the confluence between the yangtze river and the poyang lake. *Water Resources Research*, *57*(3), e2020WR028284.

Zhang, S., Jiang, B., Law, A. W. K., & Zhao, B. (2016). Large eddy simulations of 45° inclined dense jets. *Environmental Fluid Mechanics*, *16*(1), 101–121.